Beer, A. R., Turowski, J., Kirchner, J. W. (2017): Spatial patterns of erosion in a bedrock gorge. - *Journal of Geophysical Research*, *122*, 1, pp. 191—214.

DOI: http://doi.org/10.1002/2016JF003850

AGU PUBLICATIONS

JGR

Journal of Geophysical Research: Earth Surface

RESEARCH ARTICLE
10.1002/2016JF003850

Key Points:
- Spatially distributed natural bedrock erosion was measured at millimeter resolution over 2 years
- Incision, lateral, and downstream directed erosion patterns reflect the sediment tools and cover effects
- Erosion rates of surfaces depend on their position and orientation relative to the sediment flux

Correspondence to:
A. R. Beer,
alexander.beer@usys.ethz.ch

Citation:
Beer, A. R., J. M. Turowski, and J. W. Kirchner (2017), Spatial patterns of erosion in a bedrock gorge, *J. Geophys. Res. Earth Surf.*, *122*, 191–214, doi:10.1002/2016JF003850.

Received 11 FEB 2016
Accepted 1 DEC 2016
Accepted article online 7 DEC 2016
Published online 13 JAN 2017

Spatial patterns of erosion in a bedrock gorge

Alexander. R. Beer[1,2], Jens M. Turowski[3], and James W. Kirchner[1,2]

[1]Swiss Federal Institute for Forest, Snow and Landscape Research WSL, Birmensdorf, Switzerland, [2]Department of Environmental System Science, ETH Zurich, Zurich, Switzerland, [3]Helmholtzzentrum Potsdam, German Research Centre for Geosciences GFZ, Potsdam, Germany

Abstract Understanding the physical processes driving bedrock channel formation is essential for interpreting and predicting the evolution of mountain landscapes. Here we analyze bedrock erosion patterns measured at unprecedented spatial resolution (mm) over 2 years in a natural bedrock gorge. These spatial patterns show that local bedrock erosion rates depend on position in the channel cross section, height above the streambed, and orientation relative to the main streamflow and sediment path. These observations are consistent with the expected spatial distribution of impacting particles (the tools effect) and shielding by sediment on the bed (the cover effect). Vertical incision by bedrock abrasion averaged 1.5 mm/a, lateral abrasion averaged 0.4 mm/a, and downstream directed abrasion of flow obstacles averaged 2.6 mm/a. However, a single plucking event locally exceeded these rates by orders of magnitude (~100 mm/a), and accounted for one third of the eroded volume in the studied gorge section over the 2 year study period. Hence, if plucking is spatially more frequent than we observed in this study period, it may contribute substantially to long-term erosion rates, even in the relatively massive bedrock at our study site. Our observations demonstrate the importance of bedrock channel morphology and the spatial distribution of moving and static sediment in determining local erosion rates.

1. Introduction

Bedrock-alluvial gorges are sites of intense geomorphic activity and are prevalent in steep mountain ranges [*Turowski*, 2012]. Understanding the evolution of mountain landscapes depends on determining how, and how rapidly, rivers erode these gorges. Several physical processes contributing to the erosion of natural bedrock have been identified [e.g., *Whipple et al.*, 2000; *Sklar and Dietrich*, 2004; *Lamb et al.*, 2008], and their dependence on water discharge [*Venditti et al.*, 2014], on substrate characteristics [*Wohl and Achyuthan*, 2002; *Jansen et al.*, 2010; *Johnson et al.*, 2010; *Bursztyn et al.*, 2015], and on topography [*Huda and Small*, 2014; *Inoue et al.*, 2014] are currently debated.

Generally, the most important physical erosion processes are fluvial plucking, i.e., the loosening and removal of entire bedrock blocks by hydraulic forces and particle impacts, and (hydro-)abrasion, which is bedrock downwear due to impacting sediment particles [e.g., *Whipple et al.*, 2000, 2013; *Cook et al.*, 2013; *Beer and Turowski*, 2015]. A variety of erosion models have been proposed (in the following we use the word "erosion" as a generic term for all spatially undirected wear processes and specify the process at hand, as necessary). The commonly applied stream power model accounts for hydraulic forces by a dependence on water discharge and channel bed slope [*Howard and Kerby*, 1983; *Turowski*, 2012; *Lague*, 2014]. Specific effects of sediment transport have also been incorporated into models [*Sklar and Dietrich*, 2006; *Lamb et al.*, 2008; *Whipple et al.*, 2013], in particular, the observed interaction of the sediment tools and cover effects [e.g., *Sklar and Dietrich*, 2004; *Cowie et al.*, 2008; *Johnson et al.*, 2009; *Turowski and Rickenmann*, 2009; *Hobley et al.*, 2011; *Jansen et al.*, 2011; *Yanites et al.*, 2011]. These effects describe the erosive effect of mobile sediment impacting on bare bedrock (the tools effect) and the converse shielding effect of stationary sediment protecting the bedrock from abrasion (the cover effect).

The spectrum of available bedrock erosion models can be cast into generic formulas [*Whipple*, 2004; *Sklar and Dietrich*, 2006], some of which have been calibrated to specific erosional processes. For example, *Chatanantavet and Parker* [2009] focused on fractured lithology that enables plucking, while the saltation-abrasion model [*Sklar and Dietrich*, 2004] describes gradual downwear of a flat surface by bed load impacts. The saltation-abrasion model has subsequently been generalized to include the influence of abrasion by suspended load (total load erosion model [*Lamb et al.*, 2008; *Scheingross et al.*, 2014]) and more complex local

bed morphologies [*Huda and Small*, 2014]. The existing erosion models have generally been applied and compared to each other over large spatiotemporal scales [e.g., *Tomkin et al.*, 2003; *van der Beek and Bishop*, 2003; *Sklar and Dietrich*, 2006; *Hobley et al.*, 2011; *Cook et al.*, 2013], but a recent study has also focused on model assessment using high-resolution data collected during a single flood event [*Beer and Turowski*, 2015].

In parallel, laboratory studies analyzing spatiotemporal evolution of surface changes have been used to evaluate how bedrock erosion works. *Shepherd and Schumm* [1974] used a mixture of bentonite and sand material in laboratory flume experiments to describe transient formation of bedrock bed morphology with focus on inner channels (slot canyons in the active channel), and *Wohl and Ikeda* [1997] used similar experiments to study the dependency of inner channel formation on channel gradient. *Finnegan et al.* [2007] and *Johnson and Whipple* [2007, 2010] built on these results and examined the interplay between sediment availability, the tools and cover effects, and streambed width and roughness. Steady state topography and linear dependencies of channel slope and flow velocity on constant tectonic uplift were found by *Lague et al.* [2003] and *Turowski et al.* [2006], who analyzed evolving channel geometry in small-scale experiments with cohesive substrates (loess and silica) eroded by clear water flow. Recently, *Fuller et al.* [2016] highlighted the importance of streambed roughness in driving lateral erosion by deflecting sediment particles, using a weak sand-cement mixture for the walls and fixed protruding grains of various grain sizes for the bed of a laboratory flume.

Field studies of bedrock channel evolution have been conducted at various scales. Work at large spatial scales (reach scale to catchment scale) has mostly focused on long-term bedrock river evolution driven by changes in tectonics and climate [e.g., *Lavé and Avouac*, 2001; *Whittaker et al.*, 2007; *Montgomery and Korup*, 2010; *Yanites et al.*, 2010; *Jansen et al.*, 2014], while on intermediate scales (subreach scale to reach scale), studies have mostly sought to characterize site-specific dominant processes [e.g., *Lamb et al.*, 2007; *Ouimet et al.*, 2008; *Valla et al.*, 2010; *Wilson et al.*, 2013]. The tools and cover effects have been shown to be of major importance at least on intermediate scales [*Turowski et al.*, 2008; *Turowski and Rickenmann*, 2009; *Johnson et al.*, 2009, 2010; *Hobley et al.*, 2011; *Jansen et al.*, 2011; *Cook et al.*, 2013; *Beer and Turowski*, 2015; *Turowski and Bloem*, 2015]. Furthermore, local erosion can be related to factors including the sinuosity of the stream channel [*Stark et al.*, 2010] or the channel's macroroughness [*Johnson and Whipple*, 2007; *Yager et al.*, 2007; *Inoue et al.*, 2014; *Zhang et al.*, 2015]. Such morphological structures guide the bed load transport path focusing bed load impacts (and thus bank erosion) on the outsides of curved stream reaches [*Cook et al.*, 2014]. This process is reflected in the German terms for the outer and inner banks of bends — the Prallhang or "impact slope," and the Gleithang or "glide slope," respectively.

An increasing number of field studies deal with small-scale (point scale to subreach scale) short-term bedrock streambed evolution and its driving mechanisms in order to assess the plausibility of the current mechanistic concepts and process models at the appropriate resolution. *Hartshorn et al.* [2002] monitored erosion due to typhoon-driven floods along a bedrock river cross section in Taiwan using an at-a-point surveying device with micrometer resolution [*Stephenson*, 2013]. Based on the measurements of *Hartshorn et al.* [2002] and further data, *Turowski et al.* [2008] related the observed erosion patterns to bed load abrasion generated by the interplay of the sediment tools and cover effects. *Lavé and Dubille* [2011] proposed continuously recording at-a-point erosion sensors built of thin electrical resistance nets glued into in situ bedrock, which were recently shown to be able to record erosion rates during an individual event [*Beer and Turowski*, 2015; *Beer et al.*, 2015; *Turowski and Cook*, 2016] and hence can monitor the bed load tools effect. Advancing the spatial view to high-resolution surveys, *Wilson et al.* [2013] studied the morphological evolution of big boulders in the streambed using a triangulation laser scanner. They observed the downstream migration of common bedrock shapes, so-called Upstream Facing Convex Surfaces (UFCSs) [*Richardson and Carling*, 2005; *Wilson et al.*, 2013], which occur on protruding bedrock sections. These surfaces are prone to high-energy impacts by saltating bed load [*Huda and Small*, 2014], as evidenced by the abundant impact marks that are often observed on their upstream faces [*Wilson and Lave*, 2013]. Since abrasion rates by sediment impacts scale linearly with sediment transport rate [e.g., *Sklar and Dietrich*, 2001; *Beer and Turowski*, 2015; *Jacobs and Hagmann*, 2015], they likely also do so with sediment energy input [*Sklar and Dietrich*, 2004; *Huda and Small*, 2014].

The cited studies confirm that local erosion rates are strongly dependent on local erosion processes, which in turn are related to the local streambed morphology (as well as to more general factors such as lithology). Due to the competing tools and cover effects, the spatial distribution of both stationary and mobile sediment is a major control on both short-term [*Turowski et al.*, 2008; *Beer and Turowski*, 2015] and long-term [*Lague*, 2010; *Turowski et al.*, 2013] bedrock channel erosion. Hence, understanding of local bedrock surface

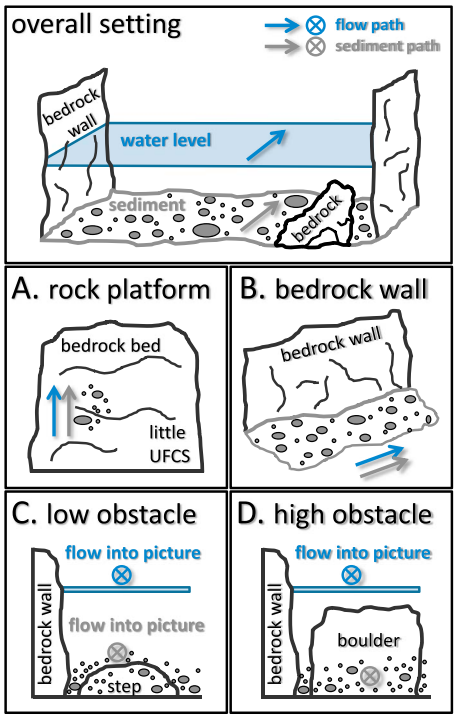

Figure 1. Sketches of Generic Morphological Shapes (GMSs) in bedrock channels, as models that illustrate expected spatial erosion patterns: (top) Definition of a generic stream cross section, showing a rectangular bedrock-alluvial channel with the paths of streamflow (blue arrow) and sediment flux (gray arrow) parallel to the walls, (a) top view of a smooth bedrock platform overflowed by streamflow and sediment, (b) lateral view of a smooth bedrock wall without an adjacent flow obstacle in the streambed, (c) downstream view along a bedrock wall adjacent to a low flow obstacle (a step), and (d) downstream view along a bedrock wall adjacent to a higher flow obstacle (a boulder), which is only slightly overflowed.

evolution dynamics is crucial for spatiotemporal upscaling and model assessment [*Huda and Small*, 2014]. However, high-resolution field measurements have so far been restricted to single flood events or individual locations in the streambed and cannot be readily generalized. Thus, there is a need for bedrock erosion measurements that have both higher spatial resolution and larger spatial coverage and that allow us to infer spatially distributed bedrock erosion rates that are temporally averaged over various flood events.

Here we present a 2 year data set of spatially distributed millimeter-scale erosion rates, measured in a natural bedrock gorge section in the Swiss Alps that is affected by hydropower-driven flood events. We use this data set to test whether the current concepts of erosional forcing can be confirmed for four generic morphological shapes of gorge topography and quantitatively analyze how bedrock erosion varies with position in the channel and orientation relative to the flow. Further, we evaluate the strengths and limitations of this high-resolution geomorphometric data set.

2. Definition of Generic Morphological Shapes (GMSs)

Diverse morphological shapes can be observed in natural bedrock streams [e.g., *Wohl et al.*, 1999; *Wohl and Merritts*, 2001; *Richardson and Carling*, 2005]. Here we define several bedrock channel configurations, which we call Generic Morphological Shapes (GMSs), to evaluate the spatial efficiency of bedrock erosion processes at intermediate scales. We are aware that there are a variety of other geometric configurations, but restrict ourselves here to these, as we think they are basic and common. As described in this section, we determine the erosion patterns we expect for each of these GMSs based on the concepts of bedrock erosion processes. In section 6, we compare these expected erosion patterns with spatial erosion measurements on comparable morphological shapes in the field and draw inferences concerning why and where erosion takes place.

We consider a rectangular straight stream reach in massive, unjointed bedrock, i.e., a semialluvial bedrock gorge [see *Turowski*, 2012], that experiences sediment throughput (cross-section view at the top part of Figure 1). The flow paths of water and sediment are generally parallel to the side walls. However, sediment cover is typically patchy and dynamically variable due to stochastic sediment transport, wall undulations (curvature), and variations in bedrock roughness [e.g., *Hodge et al.*, 2011; *Yager et al.*, 2012; *Cook et al.*, 2014]. To explore how different morphological channel configurations may influence patterns of flow, transport, and erosion, we define four GMSs with massive bedrock flow obstacles of increasing size on the streambed (Figures 1a–1d) and describe the spatial distribution of erosion expected on them.

a. *Bedrock platform*: Water and sediment flow over a planar bedrock surface. Owing to bedrock heterogeneities and turbulent sediment interactions, its initially smooth shape is expected to develop small-scale topography such as flutes [*Richardson and Carling*, 2005] due to the sediment tools effect. The upstream faces of these flutes should be preferential locations of erosion [*Wilson et al.*, 2013]. The flutes in turn guide the flow of water and sediment [*Finnegan et al.*, 2007; *Johnson et al.*, 2010], which potentially results in a

self-organized, slowly migrating pattern of flutes and their crestlines. Alternatively, if sediment transport is sufficient to bury the surface, it will shield it from erosion [*Turowski et al.*, 2008].

b. *Bedrock wall without flow obstacle*: A vertical, straight, smooth bedrock wall, without major obstacles in the nearby streambed, is laterally passed by the streamflow and sediment. Due to the "law of the wall" this bedrock wall experiences lower shear stresses than the channel center (there is a decreasing shear stress profile toward the bedrock wall [*Parker*, 1978; *Houjou et al.*, 1990]); these stresses further decrease with increasing height over the bed. The wall is exposed to relatively few sediment impacts, at least from bed load, since the main flow path of water and sediment is in the center of the stream [*Johnson and Whipple*, 2007; *Cook et al.*, 2014]. Hence, erosion rates on the wall are likely to be low and to decrease quickly with increasing height above the streambed. For high sediment concentrations causing streambed cover, however, the rate of lateral erosion should be correspondingly higher, with a peak erosion rate at the height of the sediment cover, where the most tools are available [*Hartshorn et al.*, 2002; *Turowski et al.*, 2008]. Along a wall with slight undulations, upstream facing sections of protruding parts are expected to erode faster than downstream facing parts, due to their higher exposure to sediment impacts, both from bed load and suspended load.

c. *Bedrock wall and adjacent low obstacle*: An immobile flow obstacle, such as an upstream facing step with low vertical protrusion relative to the flow depth, is situated in the streambed adjacent to a bedrock wall. Erosion is expected to be highest on the upstream side of the obstacle, due to nearly perpendicular impact angles of sediment grains and therefore maximum impact energies there [*Huda and Small*, 2014; *Wilson and Lave*, 2014]. Alluvial cover can be expected on the upstream side of the obstacle at medium or high sediment transport rates, potentially forming a ramp. This would result in constant, or even increasing, erosion rates with height over the streambed on that obstacle. Toward the wall, surface erosion rates should decline due to wall drag, as in case (b). However, sediment will be deflected toward the wall by the obstacle and the turbulence it generates. This effect likely results in higher lateral wall erosion rates than on a wall next to a sediment-covered bed (case (b), compare *Fuller et al.* [2016]).

d. *Bedrock wall and adjacent high obstacle*: A flow obstacle (e.g., a boulder) with a height on the order of the flow depth is situated beside a bedrock wall. The upstream face of the obstacle receives high-energy impacts from sediment particles, similar to the small obstacle in case (c). However, there might be a smaller number of impacts on higher regions of this obstacle, since the flow slows down near the obstacle and diverges laterally, and the bed load concentration decreases with height above the bed. Hence, we also expect decreasing erosion of the obstacle with increasing height above the bed. Erosion on the adjacent wall should be lower than in case (c), since the larger obstacle is expected to divert the flow more strongly toward the stream center, and thus reduce the energy input by impacting sediment.

On the reach scale, the assumptions outlined above for the individual GMSs imply the following: (i) bedrock bed sections should show preferential paths of sediment transport, spatially constraining vertical erosion (incision); (ii) erosion rates should be much higher in the stream center than on the walls; (iii) lateral wall erosion rates should be low in stream sections without noticeable flow obstacles on the bed; (iv) protruding bedrock in the streambed should show higher downstream directed erosion rates on upstream facing surfaces and should promote lateral wall erosion by deflecting flow and sediment transport toward the wall; and (v) erosion rates should decrease rapidly with increasing height above the common streambed height, and thus with decreasing availability of erosive tools.

3. Field Site and Data Acquisition

The Gornera stream (Canton Valais, Switzerland) drains a catchment situated between 2000 m and 4600 m altitude, near Zermatt in the Swiss Alps. Roughly 60% of its 80 km^2 drainage area is glaciated [*Farinotti et al.*, 2012]. The glacial meltwater discharge shows a strong daily cycle and transports large amounts of sediment [*Bezinge*, 1987]. The water is collected for hydropower production at an intake equipped with a sediment retention basin (UTM coordinates 32T 401665°E 5093725°N, altitude 2005 m). The sediment that collects in the retention basin is regularly flushed by opening a sluice weir and releasing the water stored in the basin, along with the current stream discharge. This procedure is termed "drawdown flushing" [*Kondolf et al.*, 2014], and we use the abbreviation "flushing" here. During the short flushing periods, the sediment-laden flow runs through the original channel downstream of the water intake. This channel is nearly dry at discharges of less than roughly 20 m^3/s, when all the stream discharge is diverted at the water intake. However, for discharges above this threshold, some water overflows the two parallel Tyrolean weirs (capacity of collection: 2×15 m^3/s)

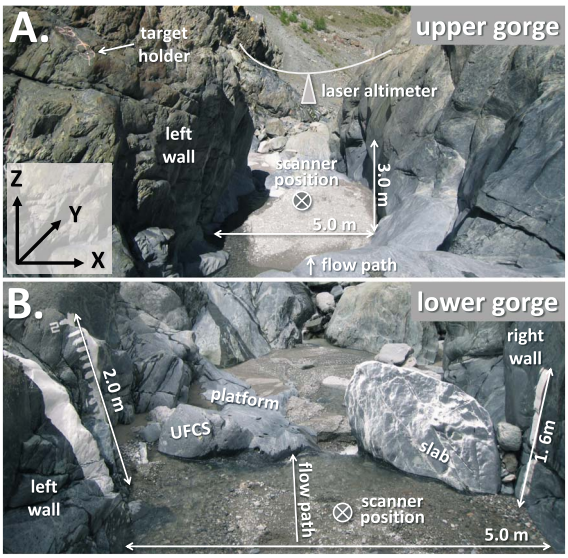

Figure 2. Overviews of the studied gorge section in the incised roche moutonnée of the Gornera stream, showing the individual study sites: (a) the upper gorge with two parallel bedrock walls and (b) the lower gorge showing the left wall, its adjacent UFCS (Upstream Facing Convex Surface), the bedrock platform, as well as the right wall and its adjacent vertical slab. Note the coordinate system defined in the inset in Figure 2a which is used to interpret the TLS data and the surface normal vector orientations.

at the water intake, resulting in flow through the natural channel. The channel bed is only sparsely vegetated and geomorphologically active during flushings due to a large supply of sediment from upstream. Both of these characteristics reflect the fact that the tongue of the Gorner Glacier receded from the location of the water intake only ~80 years ago [*Holzhauser*, 2010].

Roughly 300 m downstream of the water intake, there is a serpentinite bedrock reach that appears to be an incised roche moutonnée. This basically straight bedrock-alluvial gorge is 25 m long, 5 m to 6 m wide, and up to 8 m deep, with slightly undulating vertical rock walls. The streambed in the upper part of the gorge (Figure 2a) mainly consists of alluvium (gravel and sand of serpentinite and gneiss), which is reworked during flushings. The lower gorge (Figure 2b) features a 0.8 m high convex bedrock step on the left (henceforth called UFCS for Upstream Facing Convex Surface, due to its appearance), with a downstream bedrock platform and a 1.4 m high vertical bedrock slab on the right, both of which are overflowed during flushings.

The hydropower operator (Hydro Exploitation SA) has provided 15 min stream discharge measurements at the water intake for the 2 years of our study (2012 and 2013). A laser altimeter was mounted above the streambed in the upper gorge (Figure 2a) and recorded mean water stage at 1 min intervals. Additionally, two fixed digital cameras took pictures during the flushings, for redundant documentation of discharge heights based on painted staff gauges on the walls of both the upper and lower gorges (Figure 2b). The bedrock surfaces of the gorge were surveyed repeatedly by terrestrial laser scanning (TLS) with a Leica ScanStation C10 at a mean point spacing of 2 mm and a mean scan point accuracy of <2 mm. This accuracy is achievable for short-range scanning (<20 m distance), as verified for this scanner by our own laboratory tests, consistent with similar validation studies on a comparable instrument by *Lague et al.* [2013]. To enable accurate registration (alignment) of scans from different scanner positions or from different scan times, 30 fixed target bolts were installed on the bedrock walls of the gorge, mostly above the observed maximum flushing height (Figure 2a). These bolts allow Leica blue and white HDS surveying targets to be placed at the same positions reproducibly and avoid the need to exactly reposition the scanner at the same place in the changing topography (e.g., of the sediment bed) over time.

4. Methods

The stream discharge time series at the Gornera water intake was provided as means over 15 min intervals. However, water surface heights in the gorge during flushings showed strong fluctuations, as detected by the laser altimeter installed there, which measured at a temporal resolution of 1 min. Hence, we estimated the flushing discharge in the gorge at this higher resolution (Figure 3), to better document its range: First, we linearly interpolated the 15 min discharge rates from the water flushed out of the retention basin to 1 min resolution. For every flushing event, we then calculated dimensional conversion factors that relate the total flushed water volume with the integral of the hydrograph below the laser altimeter in the gorge. Last, these conversion factors were multiplied with the associated water surface heights from the laser altimeter, to infer the high-frequency flushing discharge in the gorge.

For analysis of spatially distributed bedrock surface erosion, we chose four study sites in the gorge (Figure 4) that exemplify the generic morphological shapes (GMSs; Figures 1a–1d). Altogether, these four study sites

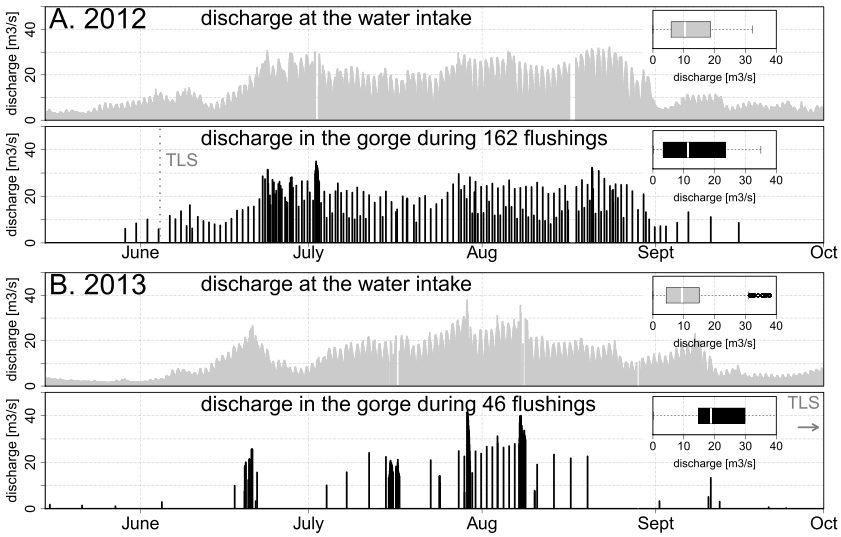

Figure 3. Both the measured discharge of the Gornera stream at the water intake (gray bars) and the calculated flushing discharge through the gorge downstream (black bars) reveal widely varying discharges for (a) the summer of 2012 and (b) the summer of 2013. Only maximum hourly discharge is given for a clearer view. Note the insets with horizontal boxplots showing the discharge distributions (1 min data interpolated from the 15 min data provided by the hydropower company). The two laser scanning dates are indicated by the acronym "TLS," whereas the second date was outside the shown time frame (in early October).

were surveyed repeatedly with TLS from three scanner positions (Table 1). Scanner Position 1 (gorge flank) was used to survey a 7 m long overflowed bedrock section in the lower gorge representing GMS (a) (smooth bedrock platform; Figure 2b). Scanner Position 2 (upper gorge) was used to survey a 9 m long wall with slight undulations and an adjacent sediment bed without flow obstacles (Figure 2a), as representative for GMS (b) (bedrock wall without flow obstacle; henceforth called left wall of the upper gorge). Finally, Scanner Position 3

Table 1. Surface Change Detection Analysis for the Four Study Sites in Figure 4, Based On TLS Measurements, Revealing Millimeter-Scale Erosion Rates Due To Bedrock Abrasion[a]

Statistics	Study Sites in the Bedrock Gorge					
Generic Morphological Shape GMS	**(a) Rock Platform**	**(b) Bedrock Wall**	**(c) Bedrock Wall and Low Obstacle**		**(d) Bedrock Wall and High Obstacle**	
Scanner position	1. Gorge flank	2. Upper gorge	3. Lower gorge			
Chosen study sites in the gorge	**Bedrock platform**	**Left wall**	**Left wall**	**UFCS[b]**	**Right wall**	**Vertical slab**
Local bed slope (%), corrected for	18.6	0.7	0.0			
Max. heigth over streambed analyzed (m)	-	3.0	3.0	0.7	3.0	1.4
Width analyzed (m)	7.0	9.0	5.0	2.1	4.1	2.3
Bedrock surface area analyzed (m^2)	20	40	22	1.3	15.6	3.2
Number of TLS targets used/skipped	5/8	5/6	4/8			
Epoch registration error, Cyclone (mm)	1.4	1.0	1.4			
Number of points analyzed	4,749,853	8,703,991	7,795,803	929,260	4,421,301	1,663,470
Mean point distance (mm)	2.1	2.1	1.7	1.2	1.9	1.4
Normal scale D for M3C2 (mm), fixed	60.0					
Mean change uncertainty, M3C2 (mm)[c]	2.9 ± 0.1	2.2 ± 0.2	3.1 ± 0.2	2.8 ± 0.1	3.0 ± 0.1	2.9 ± 0.1
Mean change (mm/2a)[c]	**-3.1 ± 2.4**	**-0.9 ± 0.9**	**-0.7 ± 2.4**	**-5.5 ± 2.9**	**-0.9 ± 1.0**	**-5.0 ± 1.2**
Average change direction	Vertical (incision)	Lateral	Lateral	Downstream	Lateral	Downstream

[a]Erosion rates and change uncertainties from the applied M3C2 algorithm are given as mean rates ± standard deviation. The generic morphological shapes (GMSs), the associated study sites, and the mean erosion rates per site section are given in bold. These mean erosion rates are also shown as red dotted lines in Figure 6.
[b]Upstream Facing Convex Surface.
[c]Mean value ± standard deviation.

(lower gorge) was used to survey a 5 m long reach (Figure 2b) with a somewhat more strongly undulating left wall, a smooth right wall, and the two different in-stream bedrock structures, the UFCS and the slab, representing GMS (c) (bedrock wall with adjacent low obstacles) and GMS (d) (bedrock wall with adjacent high obstacle).

At each of these three scanner positions, we transformed the coordinate systems of the scanned point clouds as follows, under the assumption that the average streamflow path was parallel to the walls (see the inset in Figure 2a): The *X* axis was set across the gorge perpendicular to the walls, the *Y* axis was set parallel to the mean flow path direction, inclined with the local slope of the streambed, and the *Z* axis was set pointing upward perpendicular to the other two axes. Scans analyzed here were collected in two scan epochs, June 2012 and October 2013, and surface change rates were calculated by comparing scans between the two epochs after they had been registered with one another. Although most surfaces could be seen from more than one scanner position, we only registered scans taken from the same scanner position in both epochs, in order to keep the registration errors small. From the fixed targets surrounding each scanner position, we iteratively chose a subset of targets that gave low interepoch registration errors using the commercial TLS software Leica Cyclone. In this way we avoided distortions that could be introduced by unreliable targets. Based on our own analysis and reports of *Lague et al.* [2013], aligning the scans using fixed targets yields better results for natural surfaces than, e.g., the commonly applied Iterative Closest Point algorithm for point cloud matching (ICP) [*Besl and McKay*, 1992]. Each epoch point cloud was manually cleaned to remove obvious no-bedrock data, e.g., sediment deposits or ponded water.

Change detection between the registered epoch point clouds was performed using the "Multiscale Model to Model Cloud Comparison" algorithm (M3C2) [*Lague et al.*, 2013] implemented in the free TLS software package CloudCompare. This algorithm allows at-a-point change detection on natural surfaces based on the original point cloud data, without the need for meshing them first [*Barnhart and Crosby*, 2013] and hence without introducing interpolation errors. In contrast to many other change detection algorithms, M3C2 calculates surface change along the vector that is normal to the local surface at every point of interest. This approach provides a reasonable foundation for geomorphometric analysis [*Lague et al.*, 2013] and permits quantitative analysis of the orientation of surface change in the gorge (e.g., the spatial distributions of vertical incision or lateral erosion). In settings like ours, where many surfaces are steep or vertical, conventional change detection algorithms only considering change in the *Z* direction would, e.g., misinterpret small amounts of lateral erosion as reflecting very rapid vertical incision on the gorge walls.

We initially calculated the surface normal vector for each point (in the first epoch scan point clouds) using the default multiscale search radius algorithm within M3C2 (i.e., iteratively varying the search radius $D/2$ to find neighbor points for fitting a plane; [*Lague et al.*, 2013]). This usually resulted in a robust *D* value of 0.06 m, but yielded some erroneous normal vectors, especially at ridges. We therefore calculated all surface normals by using a fixed search radius *D* of 0.06 m and then fitted a plane through the resulting disk of points. This procedure delivered reliable surface normals throughout the point clouds. The M3C2 algorithm provides an at-a-point change or distance uncertainty measure (a 95% confidence interval of detection accuracy) based on the point cloud registration error and the local surface roughness, which can be used to quantify the statistical significance of surface changes [*Lague et al.*, 2013]. However, restricting our analysis to only individual points with statistically significant change rates (which will be, for a given measurement uncertainty, the points with the largest change rates) would distort the mean rates and patterns of erosion studied here, since the typical change rates we observed between the two scan epochs are of the same magnitude as the registration errors. Thus, we used the complete change detection data sets (including nonsignificant, near-zero changes; Figure 4) to infer robust mean surface change rates, and used the calculated distance uncertainty only as a general indicator for the overall surface roughness and therefore individual scan point quality. We report surface change rates in millimeters or meters per 2 years (mm/2a or m/2a), because our survey epochs span two summers and erosion in other seasons should be negligible (since discharge and sediment transport in this glacier-fed stream are very low or zero under cold conditions).

The at-a-point surface change rates for all three study sites along the lower gorge (C. Bedrock wall with UFCS, A. Bedrock platform, and D. Bedrock wall with slab; Figure 2b) were combined to calculate mean bedrock change rates averaged over 0.05 m bins along the *X* axis, yielding an average cross-sectional profile of surface change (Figure 5). This procedure averaged values from diverse spatial surface orientations (and therefore directions of change) and from the three GMSs, since they partly overlap in the downstream (*Y*) direction.

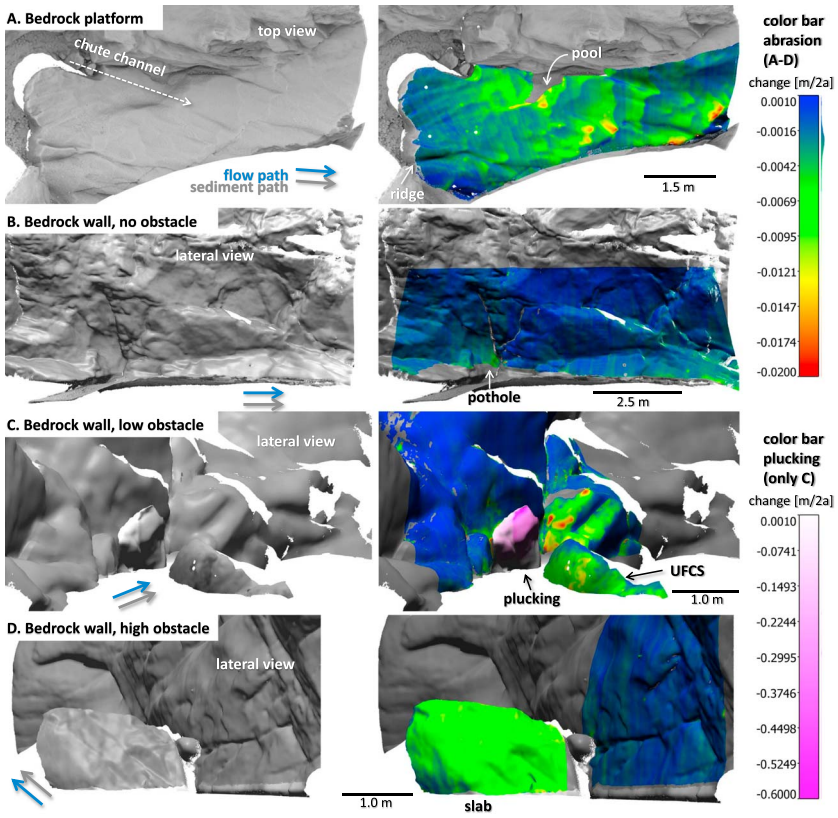

Figure 4. The spatial distributions of surface change at the four study sites (Figure 2, headlined by the represented GMS) reveal very inhomogeneous patterns. Every panel of this figure has two columns, with the left panel only showing a gray hillshade image of the study site, and the right panel overlaying spatial change detection data in color: (a) top view of the bedrock platform, (b) lateral view of the upper gorge's left bedrock wall without flow obstacles in the adjacent streambed, (c) lateral view of the lower gorge's left bedrock wall adjacent to the UFCS, and (d) lateral view of the lower gorge's right bedrock wall adjacent to the slab. Surface change was calculated for the colored regions up to a height of 3 m above the streambed. The surrounding locations where surface change was not calculated are shaded in gray for better visualization. The color bar of abrasion rates with blue to red colors applies to all the panels in the right column, whereas the pink color bar only refers to the area in Figure 4c that shows increased erosion rates due to plucking (Figure 9). Positive change rates in both ramps reflect measurement uncertainties. Blue and gray arrows indicate flow directions of streamflow and sediment, respectively. Note the different scale bars for each study site.

In addition, to examine how change rates varied with height over the streambed (Figure 6), we averaged surface change rates over height bins of 0.1 m (i.e., slices perpendicular to the *Z* axis) for all study sites except the platform, up to a height of 3.0 m (the maximum observed height of the water surface in the gorge).

To assess how surface change depends on spatial bedrock surface alignment, we first calculated the angle between each surface normal vector and the *Y* axis, which represents the average downstream flow direction. We then grouped these angles in 9° bins and averaged the surface change rates for the corresponding surface points on each of the study sites (Figure 7). To further visualize the relationships between surface orientation and surface change rates in 3-D, we used hemisphere graphs (for their construction see Appendix A) which display these relationships from different viewpoints on the individual study site data (Figure 8).

5. Results

Between the two TLS surveying epochs (June 2012 and October 2013), the gorge experienced a wide range of flushing discharges during summers (mid-May to late September; Figure 3). During this season, the glacier-fed streamflow is highest, and the sediment deposited in the retention basin needs to be cleared frequently. There was a significant decrease in the number of flushings from 162 events in 2012 (Figure 3a) to 46 events in 2013 (Figure 3b), since the hydropower company changed from a fixed daily flushing schedule to flushing on demand in order to reduce water waste. However, the total flushed volume was 75% higher in 2013

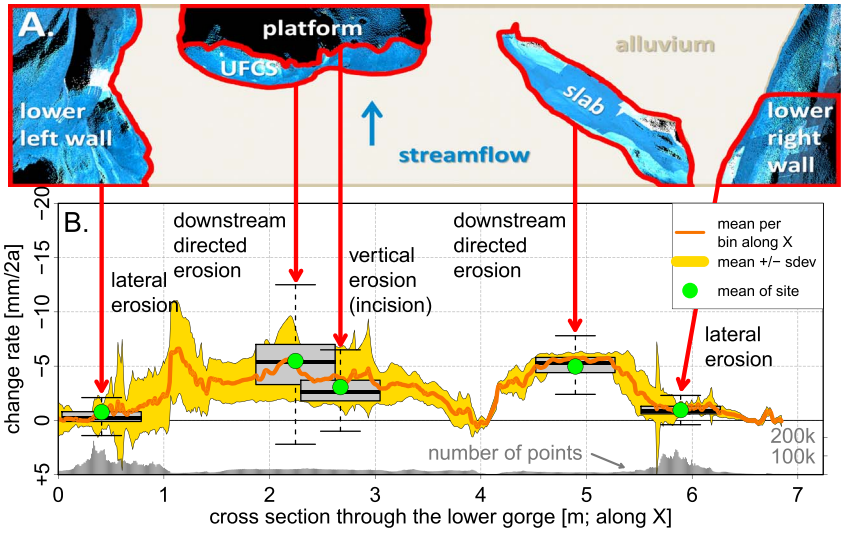

Figure 5. Variation of surface change rate with cross-sectional position in the lower gorge showing highest erosion rates near the stream center: (a) top view in the lower gorge showing several prominent features and the alluvial bed, and (b) corresponding mean erosion values along the cross section. The orange line is the mean of 0.05 m bins along the cross-section (*X* axis direction), and the surrounding yellow band is the range of the standard deviation per bin. The boxplots indicate surface change rates of the individual features at their mean locations along the cross section (*X* axis), and the green dots indicate their associated mean change rates. Note that the general directions of surface change vary among the features, as indicated by the labels (see Table 1), but the mean change rates of the orange line are binned averages over all directions. The histogram at the bottom of Figure 5b shows the number of at-a-point change detection values along *X*.

than in 2012 because flushing periods were generally longer and operated at higher streamflow (Figure 3). Thus, the bedrock surface erosion rates reported here were generated during widely varying discharges and sediment loads.

Surface change detection between the two TLS epochs was based on at least 900,000 surface points in each study site (Table 1; values for the walls and the flow obstacles in both GMS (c) and GMS (d) are listed separately). Epoch registration errors were ~1.4 mm, which is on the order of the scanning accuracy, and very small in comparison to typical morphometric field measurement errors. Therefore, and since we do not want to subjectively select or neglect parts of the results, but provide a sound evaluation of the data quality, we report and discuss the calculated distribution of spatial erosion rates including parts with problematic data.

At-a-point surface change uncertainties calculated by the M3C2 algorithm were small, averaging 2.5 mm ± 0.5 mm with a 99th percentile value of 3.5 mm, indicating that surface roughness is small and relatively homogeneous. This is reflected in the smooth visual appearance of the bedrock surfaces. All of the study sites exhibited detectable erosion rates with low standard deviations (Table 1). The walls in the upper and lower gorges showed mean lateral erosion rates on the order of submillimeters, whereas the platform was lowered (incised) by an average of ~3 mm/2a, and the upstream faces of the in-stream obstacles (the UFCS and the slab) were eroded by ~5 mm/2a.

We observed the following spatially inhomogeneous patterns of erosion at the four study sites (Figure 4): (a) a wide range of erosion values up to 12.3 mm/2a (99th percentile) were measured on the platform surface, with the highest rates found on the upstream facing sides of broad flute structures, (b) only a few areas near the streambed at the upper gorge's left wall were affected by erosion, showing maximum values of 3.4 mm/2a, (c) there was intense erosion at rates up to 12.7 mm/2a on the low-protruding UFCS and on parts of the adjacent wall, and (d) high erosion values of up to 7.0 mm/2a were also measured on the high-protruding slab, with decreasing values toward the center of the streambed, and low erosion rates on the adjacent lower right wall (99% quantile is 2.5 mm/2a). Furthermore, there was a well-defined bedrock region of at least 0.6 m^2 on the left wall of the lower gorge with erosion rates up to 534 mm/2a (Figure 4c, separate pink color bar) presumably resulting from a plucking event (Figure 9).

Another heterogeneous pattern in mean bedrock surface change can be observed along the cross section in the lower gorge (Figure 5). Erosion rates increased markedly (by 1 order of magnitude in the mean values)

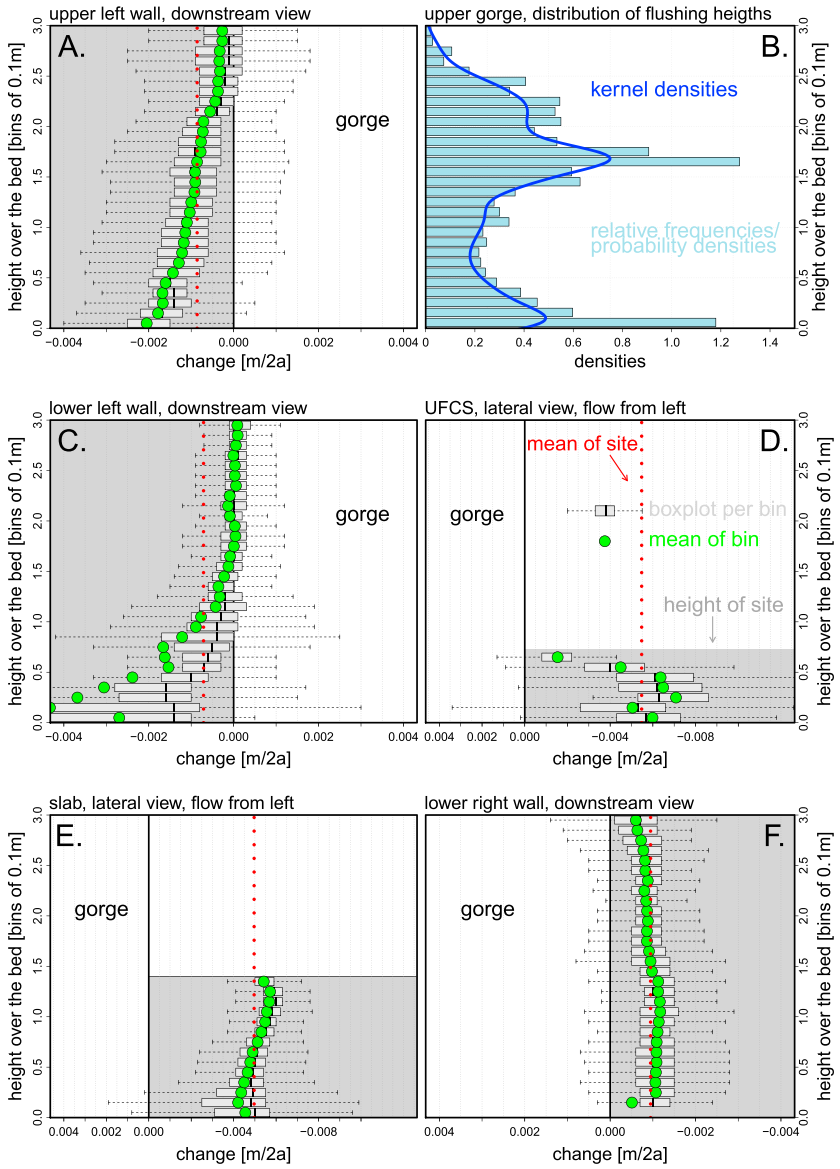

Figure 6. Variation in erosion rates with height over the streambed: (a) downstream view along the upper gorge's left wall, (b) distribution of flushing heights in the upper gorge given as a histogram and a kernel density plot, (c) downstream view along the lower gorge's left wall (excluding data from the plucking event in Figure 4c), (d) lateral view of the UFCS, (e) lateral view of the slab, and (f) downstream view along the lower gorge's right wall. Note the different viewing directions given on top of every panel. The horizontal boxplots indicate surface change for 0.1 m bins along the *Y* direction, comprising data sets of 19,000 to 320,000 points each. Boxplot widths represent interquartile range, and whisker lengths span all points within 1.5 times the interquartile range. The mean change rate per bin is additionally indicated by green dots and the total mean change rates for each site are indicated by vertical red dotted lines (see also Table 1). The gray background areas symbolize the regions of bedrock, with the value of 0.000 m/2a defining its original surface and erosion penetrating into it. Erosion rates generally decreased with height above the streambed (due to the tools effect), but are sometimes limited close to the bed (due to the cover effect).

from the walls into the streambed, but a local minimum was also detected in the streambed center between the platform and the slab (Figure 5b). This local minimum corresponds to a gap between these bedrock surfaces (Figure 5a) and thus has relatively few measurements of change rates (as shown in the histogram at the bottom of Figure 5b). The few erosion values in this gap come from an edge of the platform that is not visible in Figure 5a, but they are considered unreliable (see section 6.1 on data quality).

Figure 6 shows how bedrock erosion varies with height above the streambed for all study sites except the platform. Erosion rates on the upper gorge's left wall (Figure 6a), which has no adjacent flow obstacle in the

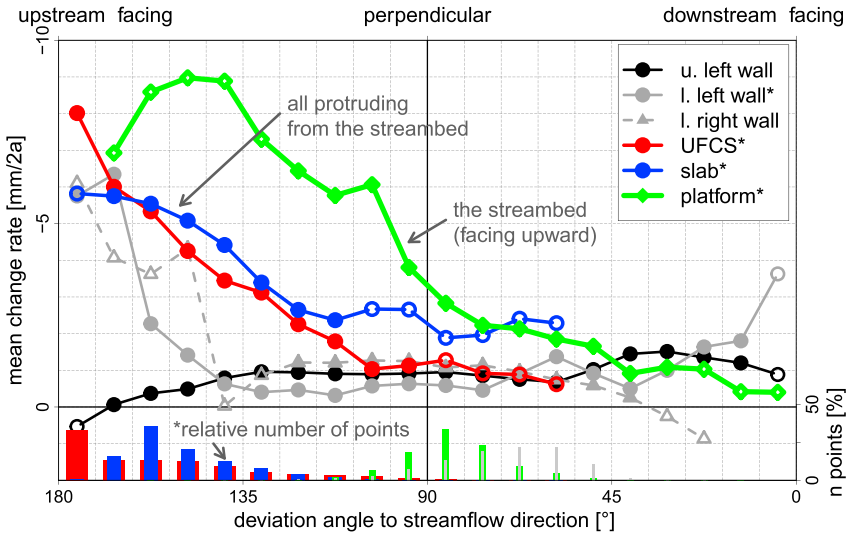

Figure 7. Mean erosion rates as a function of surface orientation relative to the streamflow direction, showing highest erosion rates on upstream facing surfaces and gradually decreasing erosion rates in the downstream direction. Note that the platform is generally facing upward, whereas all other sites protrude out of the streambed. The abbreviation "u." in the legend stands for "upper gorge" and "l." for "lower gorge". The open symbols represent binned mean change rates that are less reliable due to large laser scanner beam incidence angles and limited numbers of points (fewer than 10,000 points, see text for details). The histogram at the bottom shows the relative number of points per bin used to calculate the individual points of the lower gorge's left wall, the platform, the UFCS, and the slab.

streambed (see Figure 4a), were highest at the bottom (~2 mm/2a) and decreased almost linearly with height above the bed, approaching zero at 3.0 m, the maximum height of flushing flows. There are two slight inflections in the erosion rate profile at heights of 0.5 m and 2.2 m above the bed. These are just above the two dominant peaks in the distribution of flushing heights at this cross section (below 0.3 m and around 1.6 m; Figure 6b), suggesting a possible influence of flushing height frequency on wall erosion rates. However, the dominant pattern of surface change is the strong decrease in erosion rates with height, even though flushing flows are regularly higher than 2 m, suggesting a greater availability of erosive tools lower down in the flow.

Compared to the upper gorge's left wall, the lowermost part of the left wall next to the UFCS exhibited much higher mean erosion rates (up to 4.5 mm/2a; Figure 6c, see green dots), but comparable median erosion (see black vertical dashes in the boxplots of Figure 6c). This likely reflects the influence of a few points with very high erosion rates at the edge of the plucked block (highlighted in Figure 4c), which was excluded from our erosion rate analysis (except as detailed further below). Higher on the wall, erosion rates decreased rapidly toward zero at a height of 1.7 m above the streambed. Mean erosion of the upstream face of the UFCS (low obstacle, Figure 6d) was 8 times faster than lateral erosion on the adjacent left wall (5.5 mm/2a; Table 1) and decreased with height above the bed. Erosion rates on the higher slab were somewhat lower (5.0 mm/2a) than those on the UFCS but were more constant with height above the bed (Figure 6e). The right wall of the lower gorge (Figure 6f) showed nearly uniform lateral erosion rates of 1.0 mm/2a up to the height of 1.4 m (the height of the adjacent slab) and smoothly decreasing rates above.

Surface erosion rates, binned as a function of surface orientation relative to the streamflow direction (Figure 7), ranged from nearly zero for points facing downstream (the right edge of Figure 7) up to 9.0 mm/2a for points facing upstream (the left edge of Figure 7). The mean erosion rates reported for the most extreme surface orientations relative to the scanning beam direction at each individual study site (the open symbols in Figure 7) should be regarded with caution. These surfaces lie nearly parallel to the scanning beam, and thus their erosion rates are based on fewer, less reliable data points. For the more reliable points in Figure 7 (the full symbols), lateral erosion rates of the walls mostly ranged between 0.5 and 2.0 mm/2a. On the platform and on surfaces protruding from the streambed (the UFCS and the slab), mean erosion rates decreased markedly from upstream facing surfaces to surfaces oriented perpendicular to the streamflow (i.e., over the left half of Figure 7), but then changed much less for more downstream facing surfaces (i.e., over the right half of Figure 7). For its few surfaces oriented upstream, the platform has higher erosion rates than either the UFCS or the slab for their many upstream faces (Figure 7).

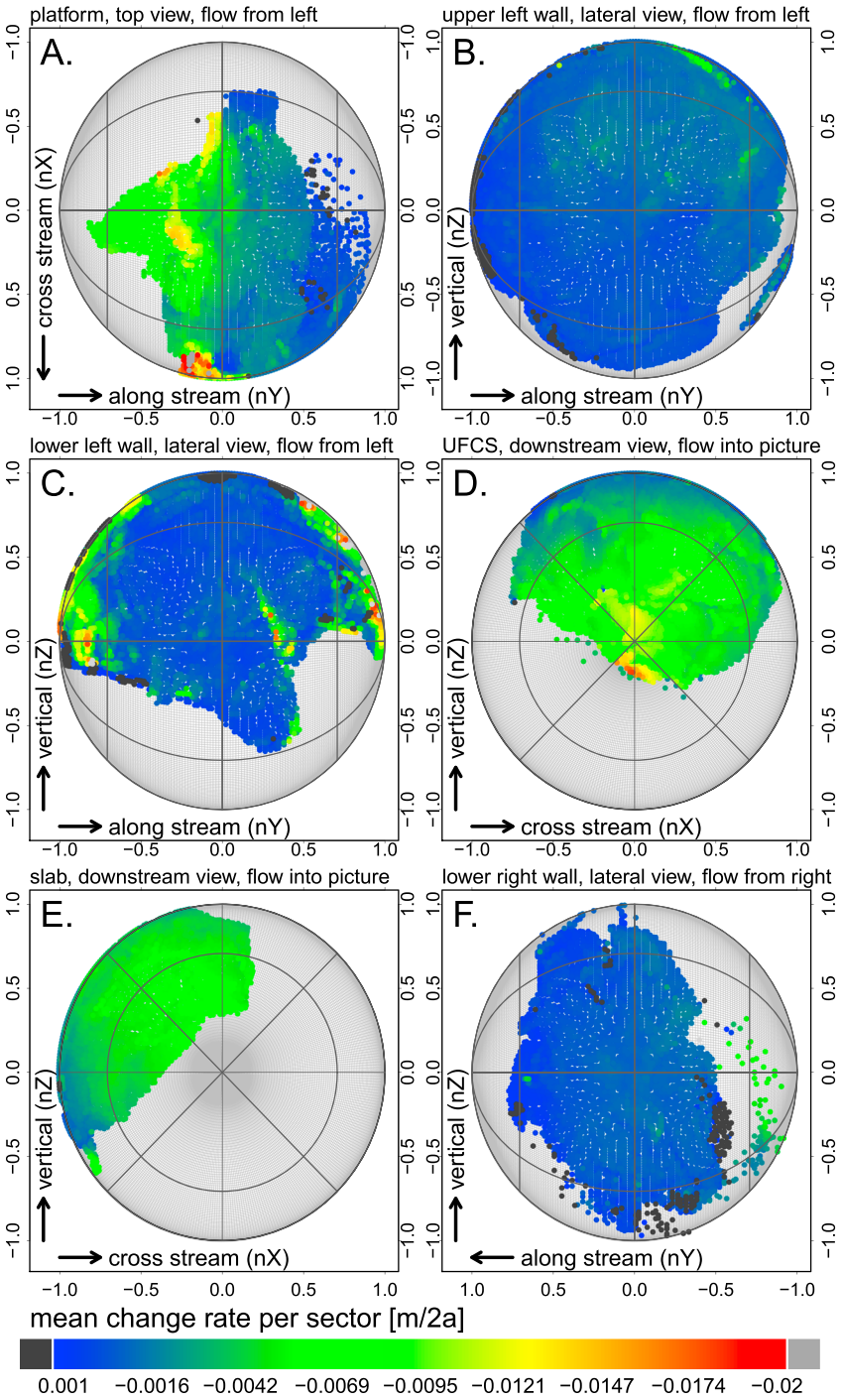

Figure 8. Hemisphere graphs showing the surface change rates of each study site as a function of spatial surface orientation (see the construction procedure in Figure A1). The highest erosion rates are observed on surfaces facing upstream and upward. The viewing directions on the hemisphere graphs shown here are consistent with the viewing directions of each panel in Figure 4: (a) hemisphere graph of the platform viewed from above, (b) graph of the upper gorge's left wall, viewed from the side, (c) graph of the lower gorge's left wall, viewed from the side, (d) graph of the UFCS, viewed in the downstream direction, (e) graph of the slab, viewed in the downstream direction, and (f) graph of the lower gorge's right wall, viewed from the side. Note the different axes and hence spatial orientations of the hemisphere graphs relative to the streamflow direction (see the inset with the coordinate system in Figure 2a). Surface change rates are given in the same color bar as Figure 4 with off-scale deposition and erosion values indicated in dark and light gray here, respectively.

Detailed relationships between surface orientation and erosion rates can be visualized with hemisphere graphs (Figure 8; see Appendix A for construction). The hemisphere graph of the platform (Figure 8a, showing a top view on the unit sphere of surface normals with flow from the left) reveals higher erosion rates on surfaces facing upstream and on those oriented perpendicular to the flow path (i.e., at the bottom of Figure 8a). Erosion rates were generally lower on the platform's downstream facing surfaces, with several spots of positive mean change (which would appear to indicate deposition in the context of change detection, indicated in black in Figure 8a). These locations of apparent deposition were mainly found at specific points on the platform's margins where cracking appears to have led to outward shifts of the bedrock. The hemisphere graph for the upper gorge's left wall (Figure 8b, lateral view with flow from the left) revealed a relatively uniform erosion pattern in the center, but noticeable apparent deposition values on strictly upstream facing surfaces (black points on the left in Figure 8b). This apparent deposition is attributable to relatively few surface points distributed across the data shown in Figure 4b, which are located at edges of undulating wall parts with their surfaces parallel to the scanning beam (boundary effect).

The lower gorge's left wall (Figure 8c, lateral view with flow from the left) generally showed higher erosion rates than the upper gorge's left wall, with both higher values on upstream facing and downstream facing surfaces. This pattern is partly attributable to the same boundary effect seen in Figure 8b. Apparent deposition values here are generally smaller and patchy with higher values also bound to the extremes of surface orientation. The hemisphere graph of the UFCS (Figure 8d, downstream view with flow into the picture) exhibited highest erosion rates in its center (i.e., surfaces facing directly upstream), decreasing uniformly as surface orientation turns more perpendicular to the flow (i.e., as one moves radially outward on the figure). The hemisphere graph of the slab (Figure 8e, downtreams view like in Figure 8d) showed a similar erosion pattern as the UFCS, with an interesting pattern at the left border region. Here erosion rates were higher at surfaces oriented upward from the streambed than surfaces oriented downward toward it, where the main streamflow (and likely sediment flow) passes by. The erosion pattern for the lower gorge's right wall (Figure 8f, lateral view, here with flow from the right) was similar to the pattern for the upper gorge's left wall (Figure 8b). However, the few points that face upstream here showed high erosion values, and there were surfaces with apparent deposition that faced perpendicular into the stream.

6. Discussion

In this section, we first assess data quality in detail to highlight potentials and limitations of our kind of high-resolution field data acquisition and address the problematic data that are sometimes observed. Then, we evaluate our findings for the four study sites compared to the erosion patterns we expected for the four Generic Morphological Shapes (GMSs, Figures 1a–1d). Based on these findings, we discuss how bedrock erosion depends on the position of a surface in the channel cross section, its height above the streambed, and its spatial orientation relative to the streamflow. Finally, we use the observed erosion patterns to discuss the potential future evolution of the gorge at the Gornera.

6.1. Data Quality

The observed bedrock erosion rates can be regarded as broadly representative 2 year means that integrate over widely varying discharge and sediment transport through the gorge. We say this because our study period comprises 2 years of typical glacially driven hydrographs and flushing events with a wide range of durations and water discharges (Figure 3). A similar broad range can be assumed for bed load transport rates and volumes, because (i) in 2012, the sediment basin was flushed daily at fixed times, with variable sediment volumes accumulating between these events, owing to variations in upstream discharge and sediment transport, (ii) in 2013, the flushings were only conducted when the sediment in the retention basin reached a fixed threshold level (and thus the intervals between the events were more variable but the sediment volumes were more constant), and (iii) the height and distribution of sediment deposits in the upper gorge (Figure 2a) varied between the flushings (as observed by the authors during several site visits), which is an indicator of varying sediment supply, at least for comparable flushing events. The stable bedrock blocks constraining the gorge section kept a generally constant sediment bed level for no-flushing periods (i.e., the height 0 m in Figure 6), with estimated locally varying sediment bed elevations between 1.0 m below, and 0.2 m above that level. Much more variable sediment bed elevations during the flushing times probably influenced water table heights in the gorge, but we did not find a strong signal by comparing the different events. Since our calculated discharge rates in the gorge are based on upstream discharge measurements, they can

be considered reliable. Comparison of the camera picture series in the upper and lower gorges revealed lower flow depths in the lower gorge and therefore higher flow velocities, potentially due to flow acceleration over the downstream sloping section of the platform. Hence, the flushing hydrographs constructed for the upper gorge (Figure 6b) are not directly transferable to the lower gorge but are qualitatively similar (with a scaling factor), since the two sites are only 14 m apart from each other.

To our knowledge, this is the first study in which erosion of natural bedrock surfaces was measured with a mean spatial resolution of 2 mm over a whole stream reach. This represents an improvement in resolution and accuracy of up to 2 orders of magnitude in comparison to previous reach-scale field studies analyzing channel change [e.g., *Lamb and Fonstad*, 2010; *Wheaton et al.*, 2010; *Cook et al.*, 2013, 2014; *Huang et al.*, 2013; *Anderson and Pitlick*, 2014]. We chose this high spatial resolution (i) to record small-scale changes in bedrock morphology, (ii) to generate spatially reliable change values by locally averaging and superimposing the TLS point footprints (which are of the same order of magnitude as the point cloud resolution), and (iii) to resolve the erosional patterns at the process scale. The overall patterns of decreasing erosion with increasing height over the streambed, cross-sectional variations in erosion rates, and surface orientation-dependent erosion rates, are plausible and robust. The large number of surface change measurements allows these trends to be defined precisely (Table 1, assuming any measurement errors are not spatially correlated). Further, the mean change uncertainties (Table 1, *Lague et al.* [2013]), which represent the 95% confidence intervals of surface changes, are smaller than the distance accuracy of single point measurements as specified by the scanner manufacturer (4 mm, which is known to be pessimistic). Thus, our measurements demonstrate that a midrange laser scanner (application distance <200 m) can detect high-resolution spatial changes on natural surfaces, at the reach scale and under field conditions. This application is complementary to smaller-scale erosion measurements at similar spatial resolution, but even higher accuracy, using close-range photogrammetry and structured-light scanning [*Wilson et al.*, 2013; *Beer et al.*, 2015].

Although single-scan data quality was generally high, occasional stripe patterns are visible in the change detection data (Figure 4a). These patterns may originate from the scanner tripod wiggling on the unstable streambed, or possibly from subtle variations in bedrock properties (density, reflectivity). These artifacts tend to average out in change detection over larger spatial scales. Further, spatially correlated change detection errors could be attributed to insufficiently fixed scanner targets, or possibly to shifts of the target bolts due to thermal effects in the bedrock. This might have led to offsets between point clouds from the two scan epochs (e.g., a shift along the (X) direction in the lower gorge, which would explain the implausibly uniform erosion rates with height at the right wall there, with apparent deposition on surfaces facing upstream; Figures 6f and 8f), or even to rotations between pairs of point clouds (which may be reflected in the erosion pattern of the upper gorge's left wall in Figure 7). These errors would only be partly reflected in epoch registration errors (Table 1). However, the availability of abundant targets per site permitted an assessment of target quality, and thus an optimized target selection with a corresponding reduction in the registration errors. Thus, we generally consider our change detection analysis to be robust.

Apparent local deposition of bedrock (positive surface change values) can be attributed to general registration errors, to the growth of cracks (as described above for the margins of the platform), and also to typical TLS measurement problems: surface contamination (sand, dust) could not be reliably removed area wide, and wet surfaces or puddles might have given erroneous values due to light refraction. An example of this problem is the 0.15 m wide zone in the center of the streambed that shows deposition on the order of 0.5 mm/2a in Figure 5b. This is where water passes between the platform and the slab during low flow (Figure 2b). Here the number of data points is small and the survey quality is poor due to surface contamination by spray and fine sediment. Further, mixed-pixel laser scanning errors (erroneous distance measurements due to averaging over blurred laser footprints [*Lichti et al.*, 2005; *Hodge*, 2010; *Nouwakpo et al.*, 2016]) likely occurred on surfaces that were nearly parallel to the laser beam, i.e., edges that were visible for the scanner only at shallow incidence angles. These edges frequently showed implausibly high positive change rates, which could be attributed to distorting fringe or boundary effects in calculating local surface normals. We therefore manually clipped obvious mixed-pixel errors at these edges. We also trimmed the borders of the change detection data sets, which corresponded to the borders of one or another point cloud where the surface normals were poorly defined. This procedure still left small regions of apparent deposition (positive change rates) in the data sets, e.g., on the right wall of the lower gorge (Figures 7 and 8f), which are further discussed later. We did not remove all these errors from the data sets, since (i) this procedure would have been elaborate (by hand, not by algorithm in the natural surfaces we analyzed), (ii) it would have been subjective, and (iii) it would have

conveyed an unrealistic impression of the data quality. However, the local phenomena of apparent deposition had little effect on the erosion patterns measured at larger scales, due to the large number of points analyzed (Table 1).

Because we surveyed naturally rough surfaces at high spatial resolution, the resulting point clouds show locally varying surface normal vectors. We calculated the local surface normals over a 0.06 m diameter footprint around each point (i.e., the normal scale D of the M3C2 algorithm). This small scale was chosen to preserve the local variations in surface orientation, even on relatively strongly curved surfaces. One consequence of this choice is that volumetric change may be overestimated along edges, where surface normals interfere with each other [*Lague et al.*, 2013], and therefore larger footprints of 0.1 m to 0.2 m would be more appropriate. However, since smooth surfaces dominate at our study sites and we measured very low change rates, such interferences are probably uncommon and hence calculation of volumetric change rates is feasible. The possibility of changes in local surface orientation due to surface erosion [*Wilson and Lave*, 2014] is beyond the scope of this study, but this effect should be small given that typical observed changes are on the order of millimeters or less, whereas the footprint for the surface normals is on the order of centimeters.

6.2. Contrasting Erosion on the Study Sites With Expectations From the GMSs

Most of the erosion patterns that were expected for the Generic Morphological Shapes (GMSs; Figures 1a to 1d) were confirmed by the measurements at our study sites (Figure 4). In the following, these measurements are discussed in detail based on the GMS concept.

a. *Bedrock platform*: The flutes on the platform surface are oriented perpendicular to the streamflow and were eroded up to their crestlines, with the highest erosion rates on their upstream facing surfaces (Figures 4a and 7). Downstream facing surfaces were also eroded, particularly for surface orientations differing by more than 45° from the streamflow direction (Figure 7). This observation on generally smooth streambed topography contrasts with the behavior reported by *Wilson et al.* [2013] and *Wilson and Lave* [2014] for larger UFCS's spanning whole boulders that showed negligible erosion on their downstream sides. On UFCS surfaces (which protrude from the streambed), the downstream energy component of the transported sediment sets the erosion rate, whereas on the upward facing surfaces of the streambed itself (such as the platform), the dominant erosive energy input is probably due to vertical forces (gravity and turbulence).
   Interestingly, on the platform, a small ridge parallel to the streamflow direction did not show noticeable erosion (bottom left side in Figure 4a), but a small pool was substantially eroded (top center in Figure 4a). Unfortunately, erosion rates could only be determined for the margins of this pool, since it contained turbid water. Together with a small flute upstream (top left in Figure 4a) this pool probably acted as a chute channel concentrating sediment transport and focusing abrasion [*Shepherd and Schumm*, 1974; *Stock et al.*, 2005; *Finnegan et al.*, 2007; *Johnson et al.*, 2010; *Nelson and Seminara*, 2011]. Also, this region of the platform contained the few points that face substantially upstream (0.5% of all points on the platform, see the green histogram at the bottom of Figure 7; their surface normals deviate more than ~120° from the streamflow direction). These points were eroded at highest mean rates, leading to the elevated erosion rates shown for the platform in Figure 7. The exact horizontal position of the platform curve on Figure 7 could vary somewhat, depending on how the streamflow direction is defined on the strongly (18.6%) inclined platform. Nevertheless, the general pattern of erosion on the platform was similar to the pattern that we expected for GMS (a) (bedrock platform).
b. *Bedrock wall without flow obstacle*: Overall, the smooth left wall in the upper gorge was only slightly eroded (Figures 4b and 7 and Table 1). There was only a weak correlation between the erosion profile with height and the distribution of flushing flow depths (Figures 6a and 6b) and erosion rates are slightly higher on upward facing surfaces than on downward facing surfaces (Figure 8b). These observations lead to several inferences:
   (i) The flushing water depth was not responsible for the bedrock erosion (by, e.g., shear detachment).
   (ii) The slight wall undulations had no direct influence on sediment impact frequency, since their protrusion into the streamflow did not lead to stronger erosion on their upstream faces. In contrast, they had a more indirect influence by generating streamflow turbulence and therefore sediment impacts, including impacts at angles deviating from the overall flow path (illustrated by the slightly increased erosion rates in a lateral pothole, left of the center in Figure 4b).
   (ii) The upward facing surfaces at the foot of the wall may have been eroded by sediment grains falling through the water column (see the bottom part of the wall in Figure 4b that is slightly inclined toward

the wall). These observations indicate that the bed load tools effect is a primary driver of lateral erosion [*Fuller et al.*, 2016]. The tools hypothesis is also consistent with the observed decrease in erosion rates with height above the bed, and particularly with the near-zero erosion rates above ~2.2 m (Figure 6a). The top regions of such flows are characterized by the highest velocities but the lowest concentrations of large abrasive sediment grains. Thus, the decrease in erosion rates with height demonstrates that the availability of tools is more important than flow velocity as a control on bedrock erosion in these profiles.

Nevertheless, erosion was detected up to the maximum height of flushing flows (Figure 6b), consistent with the visual appearance of the serpentinite bedrock. Below a height of ~3 m the surfaces have the bluish color of freshly exposed rock. Above that height, the walls are reddish due to oxidation of iron-bearing minerals. This weathered surface layer would rapidly erode if it were exposed to sediment-laden flows (i.e., if it were exposed to suspended load erosion [*Lamb et al.*, 2008; *Scheingross et al.*, 2014]). These observations are consistent with our expectations for GMS (b) (bedrock wall without in-stream obstacle), but we did not find a distinct erosion peak above the sediment bed. This would have indicated a common sediment bed level during flushings and thus a locally constrained cover effect higher than the sediment bed level during no-flushing periods (which is at 0 m elevation in Figure 6). Therefore, the high erosion rates below 0.5 m (Figure 6a) indicate a varying elevation of the sediment bed during flushings, ranging from 0.5 m down to 0.0 m, and potentially lower, consistent with variations in the flow height measurements of the laser altimeter above the gorge.

c. *Bedrock wall with adjacent low obstacle*: The left bedrock wall in the lower gorge was strongly eroded at an undulating wall section facing upstream (behind the UFCS in the center of Figure 4c), which is reflected in high mean erosion rates on the left edges of Figures 7 and 8c. This wall section is located on the left side of the small chute channel on the platform and is partially responsible for the erosion peak at ~1 m in the cross-sectional erosion profile shown in Figure 5. The high erosion rates at downstream facing sites of the wall (right edges of Figures 7 and 8c) likely arose from erroneous calculations for edges and remaining points originating from a loose cable lying on the bedrock (not visible in Figure 4c). The high mean erosion rates at the bottom of the wall (Figure 6c), and also the bright right-of-center stripe in Figure 8c, can be attributed to a locally insufficient clipping of the plucked rock region from the change detection data at this site (Figure 4c; for discussion of this plucking event, see further down). However, it was not feasible to exactly outline this region, which may not show a sharp boundary. In any case, above that plucked block, mean and median erosion rates converge again (Figure 6c). The height level with nearly zero erosion above the streambed (~1.7 m) is just below the assumed maximum level of water table heights there (~2 m, as inferred from the automated camera picture series taken in the lower gorge), which is consistent with the scaled distribution of the water table heights in Figure 6b which can be scaled for the lower gorge (see discussion above). This speaks for the same interpretation of tools-dominated lateral erosion as in case (b). The low-protruding obstacle (i.e., the UFCS) was eroded most heavily on its upstream face (Figure 5 and Table 1), with a strong dependency of erosion rates on surface orientation relative to the flow path (Figures 7 and 8d). It was likely hit by a substantial amount of flushed sediment and by the largest bed load grains, consistent with the impact marks on its rugged surface [*Wilson and Lave*, 2013, 2014]. However, the upstream facing parts of the UFCS were eroded only half as much as the platform parts that faced upstream in the chute channel (Figure 7). This could be due to (i) higher impact velocities and hence impact energies at the platform, which generally slopes downstream and does not generate a backwater effect like the UFCS, (ii) temporary cover on the upstream side of the UFCS, shielding it from impacts and reducing erosion rates there (i.e., the cover effect, as inferrable from upstream sediment deposits, observed during site visits in between the flushings), or (iii) an underestimated influence of turbulent forces on local bed load transport rates [*Schmeeckle*, 2015] and thus on the number, magnitude, and distribution of sediment impacts on the streambed.

Erosion on the UFCS focused on surfaces oriented directly against the streamflow path (i.e., in the center of Figure 8d) with the highest rates just below the center. The corresponding points are clustered at the bottom of the UFCS, which is presumably the region with the most concentrated sediment transport and thus impact energies (Figure 2b). The highest mean erosion rates (up to 7 mm/2a) were detected between 0.2 m and 0.5 m above the streambed (Figure 6d), suggesting a certain cover effect below 0.2 m. Above 0.5 m, erosion rates decreased to very low values at the crestline of the UFCS, where surfaces are oriented parallel to the streamflow direction (Figures 4c, 7, and 8d). This decrease in erosion rates may be due to sediment jumping over this area without impacts (thus reducing the tools effect).

The increased erosion at the bottom of the left wall (Figure 6c) is attributable to the adjacent UFCS, which splits the flow path and thus deflects particles into the small chute channel (left of the UFCS in Figure 2b). The cross-sectional gradient from slow erosion on the lower gorge's left wall toward rapid erosion on the UFCS (Figure 5b) provides evidence for a strong influence of the tools effect [*Turowski et al.*, 2008; *Beer and Turowski*, 2015] and qualitatively matches our expectations for GMS (c). However, quantitatively, erosion rates were expected to be much higher on the UFCS compared to the wall. Also, erosion of the upstream face of the UFCS was expected to exceed incision rates on the platform by orders of magnitude, based on bed load impact energy considerations outlined by *Huda and Small* [2014]. We attribute this pattern to (i) a temporary stable cover upstream of the UFCS (a ramp) due to the high concentration of the sediment flow during the flushings and the negligible bed slope there, and (ii) to ongoing surface erosion on the steep platform with its chute channel by overpassing sediment that does not reside there.

d. *Bedrock wall with adjacent high obstacle*: The bedrock slab situated to the right of the gorge center on average was eroded somewhat less than the UFCS (Figure 4d and Table 1). This reduction can be attributed to (i) the slab's oblique orientation to the streamflow (top view in Figure 5a) resulting in less total energy input by impacting sediment [*Huda and Small*, 2014] and to (ii) potential backwater effects arising from the slab's considerable height of 1.4 m above the streambed, slowing down both flow and sediment transport. In contrast to the other study sites, erosion rates at the slab increased slightly with height rather than decreasing (Figure 6e). This trend suggests that the cover effect here might have reached higher levels. Further, this increase clearly indicates significant sediment transport up to at least 1.4 m. The top of the slab was not visible from the scanner position in the lower gorge, so the data shown in Figure 6e do not document the decrease in erosion rates toward the slab's crest, although this is observed in measurements from the scanning position located farther downstream near the platform (1. gorge flank; Table 1). The bottom left part of the slab was less eroded than the rest (Figures 4d, 5b, and 8e). At this position there is a shift in the slab's local surface orientation from oblique to parallel to the flow path (Figure 2a), starting from the location where erosion begins to decrease in Figure 4d. This pattern reveals that this region of the slab was already shaped to a more-or-less stable morphology, i.e., parallel to the flow path of sediment passing through there.

   The uniform erosion pattern on the right wall adjacent to the slab (Figure 4d), with erosion reaching heights of more than 3.0 m above the streambed (Figure 6f), is implausible and likely results from registration errors, as stated in the section on data quality. However, at the bottom of the wall there is again an indication of the cover effect (Figure 6f), consistent with the other sites in the lower gorge. Erosion rates were more-or-less constant up to 1.4 m and decreased above this height. This height coincided with the height of the adjacent slab and the maximum erosion height of the left wall of the lower gorge (Figures 6e and 6c). Moreover, several pebbles were jammed in a ring nut screwed into the bedrock wall at 1.6 m above the bed, indicating their transport at this height. Erosion rates were higher on upstream facing surfaces (Figure 8f), but surfaces oriented perpendicular to the streamflow were also eroded substantially, probably as a result of undirected sediment impacts from the turbulent backwater behind the slab. Hence, the general qualitative erosion pattern on the right wall adjacent to the slab (Figure 7) is plausible. Our results here are somewhat in line with our expectations for GMS (d), namely, that a high-protruding flow obstacle would attenuate lateral erosion on a nearby wall (Figure 7) by diverting erosive tools toward the stream center. However, contrary to our expectations, erosion rates did not decrease with height on the slab.

6.3. General Relations Between Surface Erosion and the Flow Path

The general agreement between the expected and the observed distributions of bedrock erosion on the local scale yields insights into general erosion patterns on the reach scale. Our findings at high spatial resolution demonstrate both the tools effect and the cover effect. Our findings show the following: (i) preferential erosion paths on the streambed [*Shepherd and Schumm*, 1974; *Johnson and Whipple*, 2007, 2010], (ii) erosion rates on the order of millimeters across the stream channel, with lateral erosion rates 1 order of magnitude lower than vertical incision and downstream directed erosion rates, (iii) no general influence of obstacle height on lateral wall erosion rates, (iv) strong dependence of erosion rates on surface orientation relative to the flow, and (v) gradual decreases in erosion rates with height above the streambed (up to the maximum flushing height), with indications of a cover effect near the bed, but without correlation to flushing height frequency.

The susceptibility of surfaces to erosion was clearly related to their positions in the channel and to their orientations with respect to the streamflow and sediment flow paths. The bedrock streambed (the platform)

locally experienced the highest erosion rates (vertical incision), followed by the UFCS and the slab situated near the center of the channel (downstream directed erosion of obstacles), and then by upstream facing wall sections (strong undulations at the left wall of the lower gorge). The UFCS and the slab showed comparable linear decreases from maximum erosion rates for surfaces with 180° angles between surface normals and the streamflow direction (i.e., upstream facing surfaces) to lower values at surfaces with deviation angles of ~100° (i.e., surfaces roughly parallel to the flow). Erosion rates on both walls in the lower gorge were nonlinear functions of surface orientation, demonstrating that lateral erosion is focused on small wall patches that face upstream. This suggests that erosion tends to smooth the walls and not just widen the channel (i.e., strictly lateral erosion).

The distribution of mean erosion rates along the cross section through the lower gorge (Figure 5b) was determined based on binned averages over all local bedrock topography. These binned erosion values depend on proportions of different general surface orientations (upward facing, lateral, or upstream facing) in each bin (indicated by the average change directions, as named in Table 1). This dependence is visible, for example, in the differences between the mean cross-sectional erosion rate, and the mean erosion values of the UFCS and the platform which overlap in the streamwise direction (cf. the orange line versus the green dots between 1.5 m and 3.5 m in the transect shown in Figure 5b). Despite the variations in general surface orientations along this cross section, the overall pattern of lower erosion rates at the margins and higher rates across the center of the channel is nonetheless clearly visible in Figure 5b.

6.4. Further Evolution of the Gorge

The mean annual lateral erosion rate in the gorge was ~0.4 mm/a on the walls, the mean annual vertical incision rate was ~1.5 mm/a, and upstream faces of protruding flow obstacles were eroded at ~2.6 mm/a. (Note that these are annual rates, in contrast to the 2 year rates reported above.) These rates imply that vertical incision was 3 times faster than lateral erosion, but still 0.6 times slower than downstream directed erosion of the upstream faces of protruding obstacles. Since protruding surfaces from the walls and the bed are predominantly eroded on their upstream faces, they migrate downstream faster than the average values of lateral wall erosion [*Johnson and Whipple*, 2007; *Wilson et al.*, 2013]. The channel is therefore likely to further clear its bed of macroroughness elements and sediment deposits and evolve toward an increasingly smooth slot canyon. The measured vertical incision rate is broadly comparable to the mean physical denudation rate of the surrounding region, as inferred from catchment sediment yields (0.72 mm/a, *Schlunegger and Hinderer* [2003]).

The bedrock surfaces in the studied gorge section predominantly show the effects of abrasion by bed load and suspended load [*Hartshorn et al.*, 2002; *Johnson and Whipple*, 2007; *Scheingross et al.*, 2014], and the measured erosion rates (Table 1) reflect this process. We infer that abrasion is the spatially dominant process, because the bedrock surfaces are generally smooth, and erosion rates vary gradually in space, becoming highest on upstream facing surfaces [*Wohl et al.*, 1999; *Whipple et al.*, 2000; *Turowski et al.*, 2008; *Whipple et al.*, 2013; *Wilson and Lave*, 2014]. However, the gorge's serpentinite bedrock is inhomogeneous and exhibits local fracture zones (see Figure 2). Therefore, plucking, i.e., the loosening and removal of bedrock blocks by hydraulic forces and particle impacts, could be a considerably more efficient erosion process than abrasion at this site [*Whipple et al.*, 2000; *Hartshorn et al.*, 2002; *Whipple*, 2004]. Furthermore, the flushing events transport meter-sized boulders that are likely to constitute the major energy input to the bedrock [*Turowski et al.*, 2015] and thus the major mechanism for producing and further enhancing cracks (i.e., macroabrasion; *Whipple et al.* [2000], *Chatanantavet and Parker* [2009]).

Field evidence for the plucking process can be identified in several spots, for example, at the margins of the platform (Figure 4a, which generated the high erosion rates at the bottom of Figure 8a), or in the lateral pothole in the upper gorge's left wall (Figure 4b). The most obvious example of plucking, though, was the observation of rapid and sharply localized erosion on a 0.6 m^2 area situated in the left wall of the lower gorge (emphasized by pink coloring in Figure 4c). Here a total bedrock volume of 0.089 m^3 was removed between our two scan epochs (Figure 9), accounting for 37% of the total volume of 0.240 m^3 that was eroded from the 103 m^2 of bedrock surfaces at the four study sites. This plucked volume is an underestimate, because the lower edge of the plucked area was covered by sediment during the second TLS survey, preventing calculation of the total lost volume there (Figure 9b). Even so, the average surface erosion rate in the plucked area, 98.9 mm/a, is 279 times the abrasion rate on the other parts of the lower gorge's left wall (the plucked region

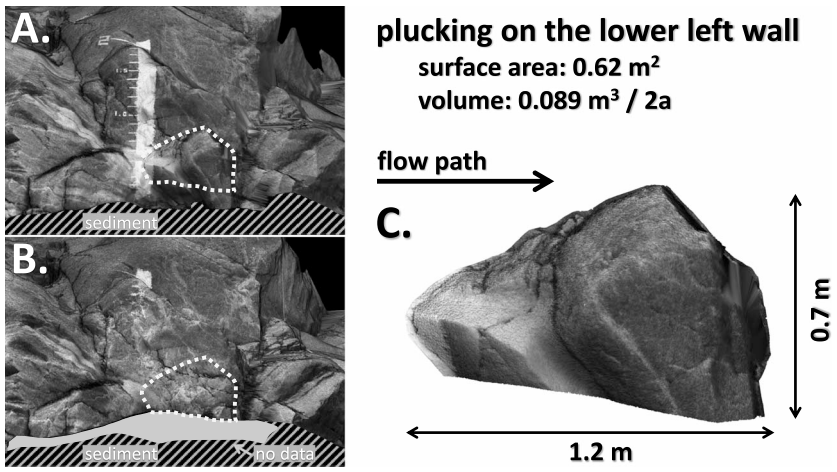

Figure 9. A block of at least 0.089 m^3 was plucked out of the lower gorge's left wall, locally generating much higher erosion rates than the surrounding rates of bedrock abrasion (Figure 4c). (a) The dashed line outlines the block in 2012, before it was plucked. (b) The same location in 2013, with the plucked block missing. The gray shadings in both panels show the streambed regions that were covered with sediment at times of surveying. In 2013, the sediment bed level was slightly higher (gray region labeled with no data in Figure 9b), preventing bedrock surface change detection at the bottom part of the wall. (c) A detailed 3D model of the plucked block.

was excluded from calculating the average rates there). Spatially averaged for our study reach and neglecting the different directions of erosion, plucking was responsible for surface removal of 0.4 mm/a and abrasion for 0.7 mm/a. Thus, particularly, if plucking events on average are more spatiotemporally frequent than the one event that we observed in our restricted 2 year study, they may be as important as (or even more important than) abrasion in accounting for the long-term evolution of the gorge [*Whipple et al.*, 2013; *Lamb et al.*, 2015]. The occurrence of comparable plucking events is probable, given (i) the strongly laterally dipping planes with their strike parallel to the streamflow direction (as visible in the upper gorge, Figure 2a), (ii) the high impact energies from the large blocks in transport, and (iii) the general prevalence of fractures in the serpentinite (Figure 2b). However, our data are inconclusive on this issue, and further studies would be needed to assess the general occurrence of plucking events.

Very high rates of inner gorge incision since the last ice age have been estimated for many glacial landscapes, but these estimates are exaggerated if inner gorges persist over multiple glacial cycles [*Montgomery and Korup*, 2010]. Our site provides an interesting illustration of this phenomenon. The gorge section that we studied has undergone several glacial cycles, becoming ice free again just 80 years ago [see *Holzhauser*, 2010, Figure 72 therein]. Yet this gorge is up to 8 m deep, over 60 times the depth that could be eroded within 80 years at our measured incision rate of 1.5 mm/a. Putting the same point differently, developing the present-day gorge would require over 5000 years of erosion at this incision rate. Therefore, the gorge was very likely influenced by glacial erosion, subglacial meltwater erosion [*Jansen et al.*, 2014], and fluvial erosion during previous ice-free periods. Although the contribution of plucking, both glacial and fluvial, is uncertain, it would likely alter the required timescales for gorge development. Nevertheless, the observed mean incision rate is consistent with rates of long-term alpine valley lowering (0.5 mm/a – 15.0 mm/a) [e.g., *Valla et al.*, 2010], suggesting that the gorge may continue to evolve as described here.

It is not clear how precisely observations made under the anthropogenic discharge regime at this site can be translated to natural conditions. The flushing events have flow rates that are comparable to natural flows, but their durations are shorter and their sediment concentrations are much higher. Despite these differences, we would expect that the qualitative patterns of bedrock erosion should be broadly transferable between the natural and the anthropogenic discharge regimes. Quantitatively, however, the lower average sediment concentrations under a natural flow regime could be expected to lead to higher erosion rates overall, because at lower concentrations, less of the sediment acts as cover and correspondingly more acts as erosive tools. Consequently, the observed erosion patterns would shift downward. Our measured erosion rates may be more quantitatively transferable for tools-dominated sites (e.g., upstream facing surfaces and those high

above the bed), because erosion rates are directly dependent on sediment impact energies [*Huda and Small*, 2014; *Beer and Turowski*, 2015; *Jacobs and Hagmann*, 2015]. For such sediment-starved conditions, the observed erosion patterns may be also qualitatively representative for larger spatiotemporal scales, since (i) they integrate over various different events, (ii) they incorporate the two probably most important erosion processes (abrasion and plucking), and (iii) they are consistent with expectations from current understanding of bedrock stream evolution that is not restricted to local and short-term dynamics. For sediment-rich conditions, where the transient spatial distribution of the cover effect will be sensitive to the actual sediment concentration, however, our observations are not transferable.

Further work will be needed to assess the quantitative generality of the observed dependence of bedrock surface erosion on in-stream morphology, including extensions to other surface geometries (e.g., larger boulders and narrower stream sections), and tests of transferability to other lithologies that are more prone to plucking [e.g., *Anton et al.*, 2015]. After additional verification, our results could be used for spatially resolved quantitative process-based predictions of bedrock erosion, e.g., through model-specific coefficients [*Sklar and Dietrich*, 2006] that account for the dependence of erosion rates on surface position and orientation.

7. Conclusions

We measured surface normal erosion rates at millimeter resolution over ~100 m^2 of bedrock in a natural gorge. This is the first application of such high-resolution measurements in such a large area. Our results generally confirmed the current understanding of how sediment transport drives bedrock erosion. The spatial pattern of erosion rates reflected surface exposure to impacting sediment grains, i.e., the tools and cover effects. Erosion was highest in the center of the gorge and smoothly decreased toward the walls. For bedrock sections protruding into the streamflow, erosion was highest on upstream facing surfaces (i.e., downstream directed erosion). On the gorge walls, lateral erosion rates decreased rapidly with increasing height above the streambed, and erosion was also slightly reduced close to the streambed due to the cover effect. On horizontal bedrock surfaces overflowed by water and sediment, surface abrasion rates were controlled by microtopography, with average vertical incision rates more than half of those observed on downstream-eroding protruding surfaces. Particularly, high abrasion rates were observed on upstream facing surfaces exposed to focused fluxes of sediment in a chute channel. Bedrock abrasion was the most widely observed erosion process. However, plucking may contribute substantially to total erosion rates even in the relatively massive bedrock at our field site, and it may be hard to measure and estimate its quantitative contribution. These findings demonstrate how bedrock topography, together with the tools and cover effects, shape the spatial pattern of bedrock erosion. Our findings highlight the importance of taking these relationships into account, for example, in designing engineered structures or modeling the evolution of steep mountainous terrain.

Appendix A: Construction of the Hemisphere Graphs

To create 2-D graphs showing the relationships between bedrock surface change and 3-D surface orientation, we used a projection technique (hemisphere graphs) inspired by the Schmidt net or stereonet drafting method that is used in structural geology to visualize features such as bedrock joint distributions [*Marshak and Mitra*, 1988]. The concept behind the hemisphere graphs was the following: If the surface normal vectors of all points from a study site (see samples in Figure A1a) are translated so that they share the same origin (0/0/0), they penetrate a unit sphere (Figure A1b), with the nY axis or the mean streamflow direction (i.e., the Y axis, see the inset in Figure 2a) being the rotation center. The surface of this sphere was subdivided in graticule sectors (here these are 1° by 1° in size, totalling 360 × 180 = 64,800 sectors). Averaging all change detection values from the surface normal vectors penetrating within each sector, we derived vectorial mean change rates (the colored polygons in Figure A1b). Cutplanes through the sphere's origin (e.g., along or perpendicular to the streamflow direction) gave two hemispheres with the streamflow crossing through the center of the cutplane. Vertical projection of the binned change rates from one of these hemispheres onto the cutplane (Lambert azimuthal equal-area projection, Figure A1c) yielded a circular area with distribution patterns of surface-averaged change rates based on surface orientation (Figure A1d). In other words, Figure A1d is a 2-D view of what is visible on the 3-D sphere in Figure A1b from one viewing direction. The choice of the cutplane direction through the unit sphere produced different viewing directions on the hemisphere. For the hemisphere graphs given in Figure 8, we chose viewing directions that are consistent with those used for each panel in Figure 4.

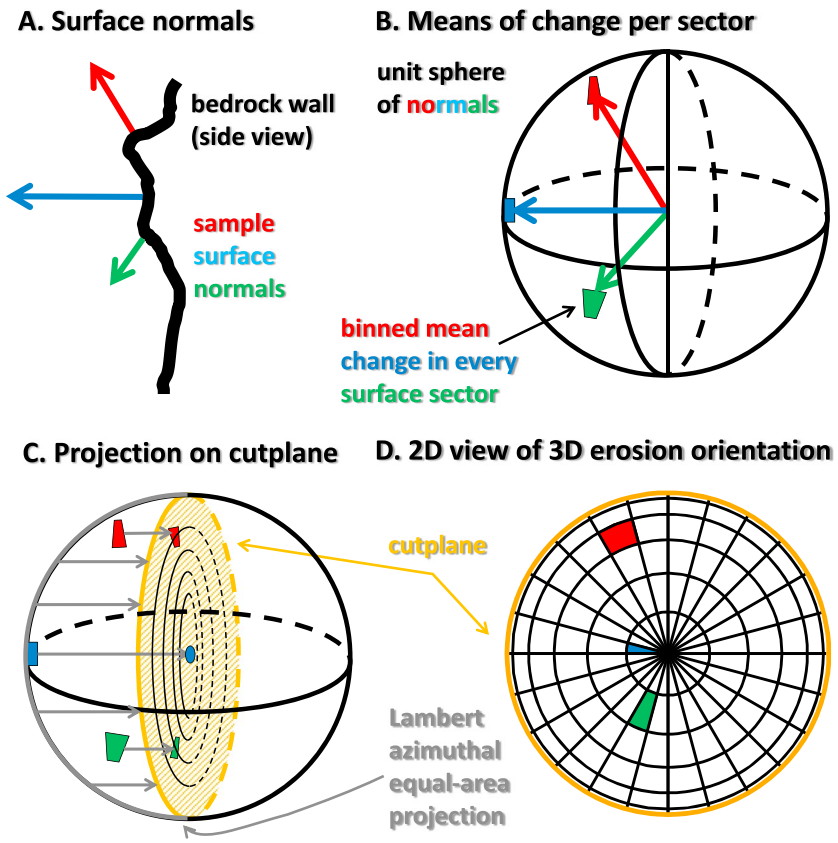

Figure A1. Construction procedure of the 2-D hemisphere graphs to show how surface change rates depend on 3-D surface orientation: (a) lateral view of a bedrock wall with surface normals originating from three sample points, (b) view of these surface normals penetrating the unit sphere around them, showing sectors over which surface change values from all penetrating surface normals are averaged, (c) Lambert azimuthal equal-area projection of one half of the unit sphere on a cutplane through the center of the unit sphere, and (d) view of this projected hemisphere on the cutplane, with colored sphere sectors indicating binned mean change rates for the points on the wall in Figure A1a, depending on their surface orientation. Note that Figure A1d actually is a 2-D view of Figure A1b, and Figure A1c is the technical construction description.

Acknowledgments
The authors thank Alexandre Badoux, Florian Heimann, Leonard Sklar, and Carlos Wyss for helpful discussions, for assistance with analysis, and for carefully reading an earlier manuscript of this paper. Phairot Chatanantavet, an anonymous referee, the Editor, and the Associate Editor greatly helped to improve the manuscript. We thank Grande Dixence SA for kindly providing access to their facilities, for permission to work in the gorge, for provision of the discharge data, and for the invaluable on-site assistance of the staff of Zmutt station. We further thank Bruno Fritschi for engineering some of the measurement equipment and Dimitri Lague for help with interpreting the M3C2 code. We appreciate the help of the following people with field work: Jean Pierre Bloem, Florian Heimann, Dirk Rieke-Zapp, Johannes Schneider, Mattia Sieber, and Thomas Weninger. For access to the data of this paper, please contact the main author. This study was supported by SNF grant 200021_132163/1.

References

Anderson, S., and J. Pitlick (2014), Using repeat lidar to estimate sediment transport in a steep stream, *J. Geophys. Res. Earth Surf.*, *119*, 621–643, doi:10.1002/2013JF002933.

Anton, L., A. E. Mather, M. Stokes, A. Munoz-Martin, and G. De Vicente (2015), Exceptional river gorge formation from unexceptional floods, *Nat. Commun.*, *6*, 7963–7963, doi:10.1038/ncomms8963.

Barnhart, T. B., and B. T. Crosby (2013), Comparing two methods of surface change detection on an evolving thermokarst using high-temporal-frequency terrestrial laser scanning, Selawik River, Alaska, *Remote Sens.*, *5*(6), 2813–2837, doi:10.3390/rs5062813.

Beer, A. R., and J. M. Turowski (2015), Bedload transport controls bedrock erosion under sediment-starved conditions, *Earth Surf. Dyn.*, *3*, 291–309, doi:10.5194/esurf-3-291-2015.

Beer, A. R., J. M. Turowski, B. Fritschi, and D. Rieke-Zapp (2015), Field instrumentation for high-resolution parallel monitoring of bedrock erosion and bedload transport, *Earth Surf. Processes Landforms*, *40*, 530–541, doi:10.1002/esp.3652.

Besl, P. J., and N. McKay (1992), A method for registration of 3-D shapes, *IEEE Trans. Pattern Anal. Mach. Intell.*, *14*(2), 239–256, doi:10.1109/34.121791.

Bezinge, A. (1987), Glacial meltwater streams, hydrology and sediment transport: The case of the Grande Dixence Hydroelectricity Scheme, in *Glacio-fluvial Sediment Transfer*, edited by A. M. Gurnell, and M. J. Clark, chap. 17, pp. 473–498, John Wiley, Chichester, U. K.

Bursztyn, N., J. L. Pederson, C. Tressler, R. D. Mackley, and K. J. Mitchell (2015), Rock strength along a fluvial transect of the Colorado Plateau—Quantifying a fundamental control on geomorphology, *Earth Planet. Sci. Lett.*, *429*, 90–100, doi:10.1016/j.epsl.2015.07.042.

Chatanantavet, P., and G. Parker (2009), Physically-based modeling of bedrock incision by abrasion, plucking, and macroabrasion, *J. Geophys. Res.*, *114*, F04018, doi:10.1029/2008JF001044.

Cook, K. L., J. M. Turowski, and N. Hovius (2013), A demonstration of the importance of bedload transport for fluvial bedrock erosion and knickpoint propagation, *Earth Surf. Processes Landforms*, *38*(7), 683–695, doi:10.1002/esp.3313.

Cook, K. L., J. M. Turowski, and N. Hovius (2014), River gorge eradication by downstream sweep erosion, *Na. Geosci.*, *7*(9), 682–686, doi:10.1038/NGEO2224.

Cowie, P. A., A. C. Whittaker, M. Attal, G. Roberts, G. E. Tucker, and A. Ganas (2008), New constraints on sediment-flux-dependent river incision: Implications for extracting tectonic signals from river profiles, *Geology*, *36*(7), 535–538, doi:10.1130/G24681A.1.

Farinotti, D., S. Usselmann, M. Huss, A. Bauder, and M. Funk (2012), Runoff evolution in the Swiss Alps: Projections for selected high-alpine catchments based on ENSEMBLES scenarios, *Hydrol. Processes*, *26*, 1909–1924, doi:10.1002/hyp.8276.

Finnegan, N. J., L. S. Sklar, and T. K. Fuller (2007), Interplay of sediment supply, river incision, and channel morphology revealed by the transient evolution of an experimental bedrock channel, *J. Geophys. Res.*, *112*, F03S11, doi:10.1029/2006JF000569.

Fuller, T. K., K. B. Gran, L. S. Sklar, and C. Paola (2016), Lateral erosion in an experimental bedrock channel: The influence of bed roughness on erosion by bed load impacts, *J. Geophys. Res. Earth Surf.*, *121*, 1084–1105, doi:10.1002/2015JF003728.

Hartshorn, K., N. Hovius, W. B. Dade, and R. L. Slingerland (2002), Climate-driven bedrock incision in an active mountain belt, *Science*, *297*, 2036–2038, doi:10.1126/science.1075078.

Hobley, D. E. J., H. D. Sinclair, S. M. Mudd, and P. A. Cowie (2011), Field calibration of sediment flux dependent river incision, *J. Geophys. Res.*, *116*, F04017, doi:10.1029/2010JF001935.

Hodge, R. A. (2010), Using simulated terrestrial laser scanning to analyse errors in high-resolution scan data of irregular surfaces, *ISPRS J. Photogramm. Remote Sens.*, *65*(2), 227–240, doi:10.1016/j.isprsjprs.2010.01.001.

Hodge, R. A., T. B. Hoey, and L. S. Sklar (2011), Bed load transport in bedrock rivers: The role of sediment cover in grain entrainment, translation, and deposition, *J. Geophys. Res.*, *116*, F04028, doi:10.1029/2011JF002032.

Holzhauser, H. (2010), *Zur Geschichte des Gornergletschers - ein Puzzle aus historischen Dokumenten und fossilen Hölzern aus dem Gletschervorfeld, Geographica Bernensia: G*, vol. 84, Univ. of Bern, Inst. of Geogr., Bern, (in German).

Houjou, K., Y. Shimizu, and C. Ishii (1990), Calculation of boundary shear stress in open channel flow, *J. Hydrosci. Hydraul. Eng.*, *8*, 21–37.

Howard, A. D., and G. Kerby (1983), Channel changes in badlands, *Geol. Soc. Am. Bull.*, *94*(6), 739–752, doi:10.1130/0016-7606(1983)94<739:CCIB>2.0.CO;2.

Huang, M. W., Y. W. Pan, and J. J. Liao (2013), A case of rapid rock riverbed incision in a coseismic uplift reach and its implications, *Geomorphology*, *184*, 98–110, doi:10.1016/j.geomorph.2012.11.022.

Huda, S. A., and E. E. Small (2014), Modeling the effects of bed topography on fluvial bedrock erosion by saltating bed load, *J. Geophys. Res. Earth Surf.*, *119*, 1222–1239, doi:10.1002/2013JF002872.

Inoue, T., N. Izumi, Y. Shimizu, and G. Parker (2014), Interaction among alluvial cover, bed roughness, and incision rate in purely bedrock and alluvial-bedrock channel, *J. Geophys. Res. Earth Surf.*, *119*, 2123–2146, doi:10.1002/2014JF003133.

Jacobs, F., and M. Hagmann (2015), Sediment bypass tunnel Runcahez: Invert abrasion 1995–2014, in *Proc. First International Workshop on Sediment Bypass Tunnels, VAW-Mitteilungen 232*, edited by R. M. Boes, pp. 211–222, Lab. of Hydraul., Hydrol. and Glaciol. (VAW), ETH Zurich, Switz.

Jansen, J. D., A. T. Codilean, P. Bishop, and T. B. Hoey (2010), Scale dependance of lithological control on topography: Bedrock channel geometry and catchment morphometry in Western Scotland, *J. Geol.*, *118*, 223–246, doi:10.1086/651273.

Jansen, J. D., D. Fabel, P. Bishop, S. Xu, C. Schnabel, and A. T. Codilean (2011), Does decreasing paraglacial sediment supply slow knickpoint retreat?, *Geology*, *39*, 543–546, doi:10.1130/G32018.1.

Jansen, J. D., A. T. Codilean, A. P. Stroeven, D. Fabel, C. Hattestrand, J. Kleman, J. M. Harbor, J. Heyman, P. W. Kubik, and S. Xu (2014), Inner gorges cut by subglacial meltwater during Fennoscandian ice sheet decay, *Nat. Commun.*, *5*, 3815, doi:10.1038/ncomms4815.

Johnson, J. P., and K. X. Whipple (2010), Evaluating the controls of shear stress, sediment supply, alluvial cover, and channel morphology on experimental bedrock incision rate, *J. Geophys. Res.*, *115*, F02018, doi:10.1029/2009JF001335.

Johnson, J. P. L., and K. X. Whipple (2007), Feedbacks between erosion and sediment transport in experimental bedrock channels, *Earth Surf. Processes Landforms*, *32*, 1048–1062, doi:10.1002/esp.1471.

Johnson, J. P. L., K. X. Whipple, L. S. Sklar, and T. C. Hanks (2009), Transport slopes, sediment cover, and bedrock channel incision in the Henry Mountains, Utah, *J. Geophys. Res.*, *114*, F02014, doi:10.1029/2007JF000862.

Johnson, J. P. L., K. X. Whipple, and L. S. Sklar (2010), Contrasting bedrock incision rates from snowmelt and flash floods in the Henry Mountains, Utah, *Geol. Soc. Am. Bull.*, *122*, 1600–1615, doi:10.1130/B30126.1.

Kondolf, G. M., et al. (2014), Sustainable sediment management in reservoirs and regulated rivers: Experiences from five continents, *Earth's Future*, *2*(5), 256–280, doi:10.1002/2013EF000184.

Lague, D. (2010), Reduction of long-term bedrock incision efficiency by short-term alluvial cover intermittency, *J. Geophys. Res.*, *115*, F02011, doi:10.1029/2008JF001210.

Lague, D. (2014), The stream power river incision model: Evidence, theory and beyond, *Earth Surf. Processes Landforms*, *39*, 38–61, doi:10.1002/esp.3462.

Lague, D., A. Crave, and P. Davy (2003), Laboratory experiments simulating the geomorphic response to tectonic uplift, *J. Geophys. Res.*, *108*(2), 2008, doi:10.1029/2002JB001785.

Lague, D., N. Brodu, and J. Leroux (2013), Accurate 3D comparison of complex topography with terrestrial laser scanner: Application to the Rangitikei canyon (NZ), *ISPRS J. Photogramm. Remote Sens.*, *82*, 10–26, doi:10.1016/j.isprsjprs.2013.04.009.

Lamb, M. P., and M. A. Fonstad (2010), Rapid formation of a modern bedrock canyon by a single flood event, *Nat. Geosci.*, *3*, 477–481, doi:10.1038/ngeo894.

Lamb, M. P., A. D. Howard, W. E. Dietrich, and J. T. Perron (2007), Formation of amphitheater-headed valleys by waterfall erosion after large-scale slumping on Hawai'i, *Geol. Soc. Am. Bull.*, *119*(7–8), 805–822, doi:10.1130/B25986.1.

Lamb, M. P., W. E. Dietrich, and L. S. Sklar (2008), A model for fluvial bedrock incision by impacting suspended and bed load sediment, *J. Geophys. Rese.*, *113*, F03025, doi:10.1029/2007JF000915.

Lamb, M. P., N. J. Finnegan, J. S. Scheingross, and L. S. Sklar (2015), New insights into the mechanics of fluvial bedrock erosion through flume experiments and theory, *Geomorphology*, *244*, 33–55, doi:10.1016/j.geomorph.2015.03.003.

Lavé, J., and J. P. Avouac (2001), Fluvial incision and tectonic uplift across the Himalayas of central Nepal, *J. Geophys. Res.*, *106*(B11), 26,561–26,591, doi:10.1029/2001JB000359.

Lavé, J., and M. Dubille (2011), Real-time measurements and modelling of bedrock river erosion along two rivers of the Frontral Himalaya, Geophysical Research Abstracts Vol. 13, EGU2011-8108 presented at 2011 EGU General Assembly, Vienna, Austria, 3–8 Apr.

Lichti, D. D., S. J. Gordon, and T. Tipdecho (2005), Error models and propagation in directly georeferenced terrestrial laser scanner networks, *J. Surv. Eng.-ASCE*, *131*(4), 135–142, doi:10.1061/(ASCE)0733-9453(2005)131:4(135).

Marshak, S., and G. Mitra (1988), *Basic Methods of Structural Geology*, Prentice Hall, New Jersey.

Montgomery, D. R., and O. Korup (2010), Preservation of inner gorges through repeated Alpine glaciations, *Nat. Geosci.*, *4*, 62–67, doi:10.1038/NGEO1030.

Nelson, P. A., and G. Seminara (2011), Modeling the evolution of bedrock channel shape with erosion from saltating bed load, *Geophys. Res. Lett.*, *38*, L17406, doi:10.1029/2011GL048628.

Nouwakpo, S., M. Weltz, and K. McGwire (2016), Assessing the performance of structure-from-motion photogrammetry and terrestrial lidar for reconstructing soil surface microtopography of naturally vegetated plots, *Earth Surf. Processes Landforms*, *41*, 308–322, doi:10.1002/esp.3787.

Ouimet, W. B., K. X. Whipple, B. T. Crosby, J. P. Johnson, and T. F. Schildgen (2008), Epigenetic gorges in fluvial landscapes, *Earth Surf. Processes Landforms*, *33*, 1993–2009, doi:10.1002/esp.1650.

Parker, G. (1978), Self-formed straight rivers with equilibrium banks and mobile bed. Part 2. The gravel river, *J. Fluid Mech.*, *89*, 127–146, doi:10.1017/S0022112078002505.

Richardson, K., and P. Carling (2005), *A typology of sculpted forms in open bedrock channels*, Geol. Soc. of Am., Boulder, Colo.

Scheingross, J. S., F. Brun, D. Y. Lo, K. Omerdin, and M. P. Lamb (2014), Experimental evidence for fluvial bedrock incision by suspended and bedload sediment, *Geology*, *42*(6), 523–526, doi:10.1130/G35432.1.

Schlunegger, F., and M. Hinderer (2003), Pleistocene/holocene climate change, re-establishment of fluvial drainage network and increase in relief in the Swiss Alps, *Terra Nova*, *15*(2), 88–95, doi:10.1046/j.1365-3121.2003.00469.x.

Schmeeckle, M. (2015), The role of velocity, pressure, and bed stress fluctuations in bed load transport over bed forms: Numerical simulation downstream of a backward-facing step, *Earth Surf. Dyn.*, *3*, 105–112, doi:10.5194/esurf-3-105-2015.

Shepherd, R. G., and S. A. Schumm (1974), Experimental study of river incision, *Geol. Soc. Am. Bull.*, *85*(2), 257–268, doi:10.1130/0016-7606(1974)85<257:ESORI>2.0.CO;2.

Sklar, L. S., and W. E. Dietrich (2001), Sediment and rock strength controls on river incision into bedrock, *Geology*, *29*(12), 1087–1090, doi:10.1130/0091-7613(2001)029<1087:SARSCO>2.0.CO;2.

Sklar, L. S., and W. E. Dietrich (2004), A mechanistic model for river incision into bedrock by saltating bed load, *Water Resour. Res.*, *40*, W06301, doi:10.1029/2003WR002496.

Sklar, L. S., and W. E. Dietrich (2006), The role of sediment in controlling steady-state bedrock channel slope: Implications of the saltation-abrasion incision model, *Geomorphology*, *82*, 58–83, doi:10.1016/j.geomorph.2005.08.019.

Stark, C. P., J. R. Barbour, Y. S. Hayakawa, T. Hattanji, N. Hovius, H. Chen, C.-W. Lin, M.-J. Horng, K.-Q. Xu, and Y. Fukahata (2010), The climatic signature of incised river meanders, *Science*, *327*, 1497–1501, doi:10.1126/science.1184406.

Stephenson, W. (2013), The micro and traversing erosion meter, in *Treatise in Geomorphology: Methods in Geomorphology*, vol. 14.14, edited by A. Switzer and D. M. Kennedy, pp. 164–169, Elsevier, Amsterdam.

Stock, J. D., D. R. Montgomery, B. D. Collins, W. E. Dietrich, and L. Sklar (2005), Field measurements of incision rates following bedrock exposure: Implications for process controls on the long profile of valleys cut by rivers and debris flows, *Geol. Soc. Am. Bull.*, *117*(11–12), 174–194, doi:10.1130/B25560.1.

Tomkin, J. H., M. T. Brandon, F. J. Pazzaglia, J. R. Barbour, and S. D. Willett (2003), Quantitative testing of bedrock incision models for the Clearwater River, NW, Washington State, *J. Geophys. Res.*, *108*(B6), 2308, doi:10.1029/2001JB000862.

Turowski, J. M. (2012), Semi-alluvial channels and sediment-flux-driven bedrock erosion, in *Gravel Bed Rivers: Processes, Tools, Environments*, edited by M. Church, P. Biron, and A. Roy, chap. 29, pp. 401–416, John Wiley, Chichester, U. K., doi:10.1002/9781119952497.

Turowski, J. M., and J.-P. Bloem (2015), The influence of sediment thickness on energy delivery to the bed by bedload impacts, *Geod. Acta*, *28*, 199–208, doi:10.1080/09853111.2015.1047195.

Turowski, J. M., and K. L. Cook (2016), Field techniques for measuring bedrock erosion and denudation, *Earth Surf. Processes Landforms*, doi:10.1002/esp.4007.

Turowski, J. M., and D. Rickenmann (2009), Tools and cover effects in bedload transport observations in the Pitzbach, Austria, *Earth Surf. Processes Landforms*, *34*, 26–37, doi:10.1002/esp.1686.

Turowski, J. M., D. Lague, A. Crave, and N. Hovius (2006), Experimental channel response to tectonic uplift, *J. Geophys. Res.*, *111*, F03008, doi:10.1029/2005JF000306.

Turowski, J. M., N. Hovius, M.-L. Hsieh, D. Lague, and M.-C. Chen (2008), Distribution of erosion across bedrock channels, *Earth Surf. Processes Landforms*, *33*, 353–363, doi:10.1002/esp.1559.

Turowski, J. M., A. Badoux, J. Leuzinge, and R. Hegglin (2013), Large floods, alluvial overprint, and bedrock erosion, *Earth Surf. Processes Landforms*, *38*, 947–958, doi:10.1002/esp.3341.

Turowski, J. M., C. Wyss, and A. R. Beer (2015), Grain size effects on energy delivery to the stream bed and links to bedrock erosion, *Geophys. Res. Lett.*, *42*, 1775–1780, doi:10.1002/2015GL063159.

Valla, P. G., P. A. van der Beek, and D. Lague (2010), Fluvial incision into bedrock: Insights from morphometric analysis and numerical modeling of gorges incising glacial hanging valleys (Western Alps, France), *J. Geophys. Res.*, *115*, F02010, doi:10.1029/2008JF001079.

van der Beek, P., and P. Bishop (2003), Cenozoic river profile development in the upper Lachlan catchment (SE Australia) as a test of quantitative fluvial incision models, *J. Geophys. Res.*, *108*(B6), 2309, doi:10.1029/2002JB002125.

Venditti, J. G., C. D. Rennie, J. Bomhof, R. W. Bradley, M. Little, and M. Church (2014), Flow in bedrock canyons, *Nature*, *513*(7519), 534–537, doi:10.1038/nature13779.

Wheaton, J. M., J. Brasington, S. E. Darby, and D. A. Sear (2010), Accounting for uncertainty in DEMs from repeat topographic surveys: Improved sediment budgets, *Earth Surf. Processes Landforms*, *35*(2), 136–156, doi:10.1002/esp.1886.

Whipple, K. X. (2004), Bedrock rivers and the geomorphology of active orogens, *Annu. Rev. Earth Planet. Sci.*, *32*, 151–185, doi:10.1146/annurev.earth.32.101802.120356.

Whipple, K. X., G. S. Hancock, and R. S. Anderson (2000), River incision into bedrock: Mechanics and relative efficacy of plucking, abrasion, and cavitation, *Geol. Soc. Am. Bull.*, *112*(3), 490–503, doi:10.1130/0016-7606(2000)112<0490:RIIBMA>2.3.CO;2.

Whipple, K. X., R. A. DiBiase, and B. T. Crosby (2013), Bedrock rivers, in *Treatise in Geomorphology: Methods in Geomorphology*, vol. 9.28, edited by A. Switzer and D. M. Kennedy, pp. 550–573, Elsevier, Amsterdam.

Whittaker, A. C., P. A. Cowie, M. Attal, G. E. Tucker, and G. P. Roberts (2007), Contrasting transient and steady-state rivers crossing active normal faults: New field observations from the Central Apennines, Italy, *Basin Res.*, *19*, 529–556, doi:10.1111/j.1365-2117.2007.00337.x.

Wilson, A., and J. Lave (2013), The legacy of impact conditions in morphometrics of percussion marks on fluvial bedrock surfaces, *Geomorphology*, *186*, 174–180, doi:10.1016/j.geomorph.2012.12.033.

Wilson, A., and J. Lave (2014), Convergent evolution of abrading flow obstacles: Insights from analogue modelling of fluvial bedrock abrasion by coarse bedload, *Geomorphology*, *208*, 207–224, doi:10.1016/j.geomorph.2013.11.024.

Wilson, A., N. Hovius, and J. M. Turowski (2013), Upstream facing convex surfaces: Bedrock bedforms produced by fluvial bedload abrasion, *Geomorphology*, *180–181*, 187–204, doi:10.1016/j.geomorph.2012.10.010.

Wohl, E. E., and H. Achyuthan (2002), Substrate influences on incised-channel morphology, *J. Geol.*, *110*, 115–120, doi:10.1086/324207.

Wohl, E. E., and H. Ikeda (1997), Experimental simulation of channel incision into a cohesive substrate at varying gradients, *Geology*, *25*(4), 295–298, doi:10.1130/0091-7613(1997)025<0295:ESOCII>2.3.CO;2.

Wohl, E. E., and D. M. Merritts (2001), Bedrock channel morphology, *Geol. Soc. Am. Bull.*, *113*, 1205–1212, doi:10.1130/0016-7606(2001)113<1205:BCM>2.0.CO;2.

Wohl, E. E., D. M. Thompson, and A. J. Miller (1999), Canyons with undulating walls, *Geol. Soc. Am. Bull.*, *111*, 949–959, doi:10.1029/2005JF000406.

Yager, E. M., J. W. Kirchner, and W. E. Dietrich (2007), Calculating bed load transport in steep boulder bed channels, *Water Resour. Res.*, *43*, W07418, doi:10.1029/2006WR005432.

Yager, E. M., W. E. Dietrich, J. W. Kirchner, and B. W. McArdell (2012), Patch dynamics and stability in steep, rough streams, *J. Geophys. Res.*, *117*, F02010, doi:10.1029/2011FJ002253.

Yanites, B. J., G. E. Tucker, K. J. Mueller, Y.-G. Chen, T. Wilcox, S.-Y. Huang, and K.-W. Shi (2010), Incision and channel morphology across active structures along the Peikang River, central Taiwan: Implications for the importance of channel width, *Geol. Soc. Am. Bull.*, *122*(7/8), 1192–1208, doi:10.1130/B30035.1.

Yanites, B. J., G. E. Tucker, H.-L. Hsu, C.-C. Chen, Y.-G. Chen, and K. J. Mueller (2011), The influence of sediment cover variability on long-term river incision rates: An example from the Peikang River, central Taiwan, *J. Geophys. Res.*, *116*, F03016, doi:10.1029/2010JF001933.

Zhang, L., G. Parker, C. P. Stark, T. Inoue, E. Viparelli, X. Fu, and N. Izumi (2015), Macro-roughness model of bedrock-alluvial river morphodynamics, *Earth Surf. Dyn.*, *3*, 113–138, doi:10.5194/esurf-3-113-2015.